2014

Characterization of DP600 Steel Subject to Electrohydraulic Forming

Brent McCallum
University of Windsor

Characterization of DP600 Steel Subject to Electrohydraulic Forming

By

Brent McCallum

A Thesis

Submitted to the Faculty of Graduate Studies

through the Department of Mechanical, Automotive, and Materials Engineering

in Partial Fulfillment of the Requirements for

the Degree of Master of Applied Science

at the University of Windsor

Windsor, Ontario, Canada

2014

Characterization of DP600 Steel Subject to Electrohydraulic Forming

by

Brent McCallum

APPROVED BY:

_____

V. Stoilov
Department of Mechanical, Automotive, and Materials Engineering

_____

A. Edrisy
Department of Mechanical, Automotive, and Materials Engineering

_____

R.J. Bowers, Co-Advisor
Department of Mechanical, Automotive, and Materials Engineering

_____

D.E. Green, Co-Advisor
Department of Mechanical, Automotive, and Materials Engineering

26 August 2014

AUTHOR'S DECLARATION OF ORIGINALITY

I hereby certify that I am the sole author of this thesis and that no part of this thesis has been published or submitted for publication elsewhere.

I certify that, to the best of my knowledge, my thesis does not infringe upon anyone's copyright nor violate any proprietary rights and that any ideas, techniques, quotations, or any other material from the work of other people included in my thesis, published or otherwise, are fully acknowledged in accordance with the standard referencing practices. Furthermore, to the extent that I have included copyrighted material that surpasses the bounds of fair dealing within the meaning of the Canada Copyright Act, I certify that I have obtained a written permission from the copyright owner(s) to include such material(s) in my thesis and have included copies of such copyright clearances to my appendix.

I declare that this is a true copy of my thesis, including any final revisions, as approved by my thesis committee and the Graduate Studies office, and that this thesis has not been submitted for a higher degree to any other University or Institution.

ABSTRACT

Electrohydraulic forming (EHF) is a manufacturing technique that transforms electrical energy into work. In EHF, a shockwave is produced as a result of a high-voltage electrical discharge between two electrodes in a water chamber, which travels through water toward the sheet and forms it into the final shape at high velocity. Strain rates can reach 10^4 s^{-1} in EHF. DP600 dual phase steel was formed in the Nakazima test in quasi-static (QS) condition, and EHF, performed without a mating die (free forming) and using a 34° conical die (die forming). The sheets were etched with a grid prior to testing to determine strains across each specimen. Analysis of voids was carried out to investigate the micro-mechanisms of failure in DP600 steel formed in these three processes. Nakazima specimens exhibited uniform strain behaviour up to 0.65 effective strain; EHFF up to 0.45 effective strain; and EHDF up to 0.7 effective strain.

ACKNOWLEDGEMENTS

It would not be possible for me to be at this stage in my education without the guidance and support of my advisors, Dr. Daniel E. Green and Dr. Randy J. Bowers. Through their extensive expertise and constant support, I have developed and refined the skills to find success in my career. I am very grateful for the opportunity and experience offered to me.

Next, I would like to thank Alan Gillard of Ford Motor Company for his valuable assistance in the electrohydraulic forming trials in Dearborn, Michigan. I would also like to thank Dr. Kevin Boyle and Lucian Blaga at CanmetMATERIALS in Hamilton, Ontario for arranging and performing the quasi-static Nakazima tests. The tests performed at these facilities provided the specimens for this research project, and discussions with these individuals yielded valued insight.

It must be acknowledged that this project would not have been possible without the Automotive Partnership of Canada and the project partners, including: Ford Motor Company, ArcelorMittal Dofasco, Amino North America Corporation, CanmetMATERIALS, the University of Waterloo, and the University of Windsor.

Finally, I would like to thank the Subcommittee on Academic Matters for being a frequent source of moral support and intellectual discussion throughout my degree.

TABLE OF CONTENTS

List of Tables

List of Figures

Chapter 1 :

Introduction

With the automotive industry making a push to decrease vehicle mass to reduce fuel consumption, higher strength steels are being employed with greater frequency in vehicles for structural components. Higher strength steel allows for thinner sections of components, which results in lower vehicle mass and, as a result, improved fuel economy [1]. Dual phase steels have been used with increased frequency in recent years because of their superior strength and ductility compared to other steels. The desire is often to opt for a higher strength steel or higher ductility metal such as aluminum or magnesium; dual phase steels, however, offer the benefits of both classes of metals at a reasonable cost.

Cost savings are also sought after in forming operations as well, which has driven industrial research into alternatives to traditional stamping and drawing. High strain rate forming operations are one such research area of interest to automotive and manufacturing companies. One of these methods is electrohydraulic forming, a type of forming process that has been researched since the 1960's [2]. It has been targeted in recent years for its potential to increase the formability of sheet materials already in use. Electrohydraulic forming offers the benefits of requiring less equipment to operate, fewer forming steps, and increased formability of standard materials that are already in use in industry. These benefits are attractive to automotive researchers today.

1.1 Objectives of Research

The aim of the current research is to understand the effect of the high strain rate electrohydraulic forming process on DP600 sheet steel. DP600 is targeted as a viable production quality alloy that already has applications in automotive bodies. It was chosen by Ford for trials in the electrohydraulic forming process to test the extent to which the process can enhance the formability of dual phase steels.

In particular, this work characterized the microstructure of the steel before and after electrohydraulic forming, and then compared it to the microstructure after quasi-static forming. Two electrohydraulic forming setups were studied: free-forming and die-forming. The microstructures from these three forming process variants were studied and characterized with a particular focus on the mechanisms that led to or resisted fracture. The microstructures of the specimens were examined using optical microscopy and scanning electron microscopy to quantitatively and qualitatively observe these mechanisms or the artifacts thereof.

For this particular grade of steel to be viable in industrial applications of this forming process, evidence was required of its superior damage accommodation in electrohydraulic forming compared to that observed in conventional quasi-static forming.

Chapter 2 :

Literature Review

2.1 Dual Phase Steels

Dual phase (DP) steels have been used in automotive applications since the early 1970s. They are produced from low carbon steels (0.05-0.2 wt%) in a process of either intercritical annealing or sequential quenching, as described in the following section. They are most desirable for their combination of good ductility, elongation, and strength characteristics [3]. The microstructure of DP steel consists of a soft ferrite matrix with interspersed hard martensite islands, Figure 2.1, which give the steel its ductility and strength, respectively.

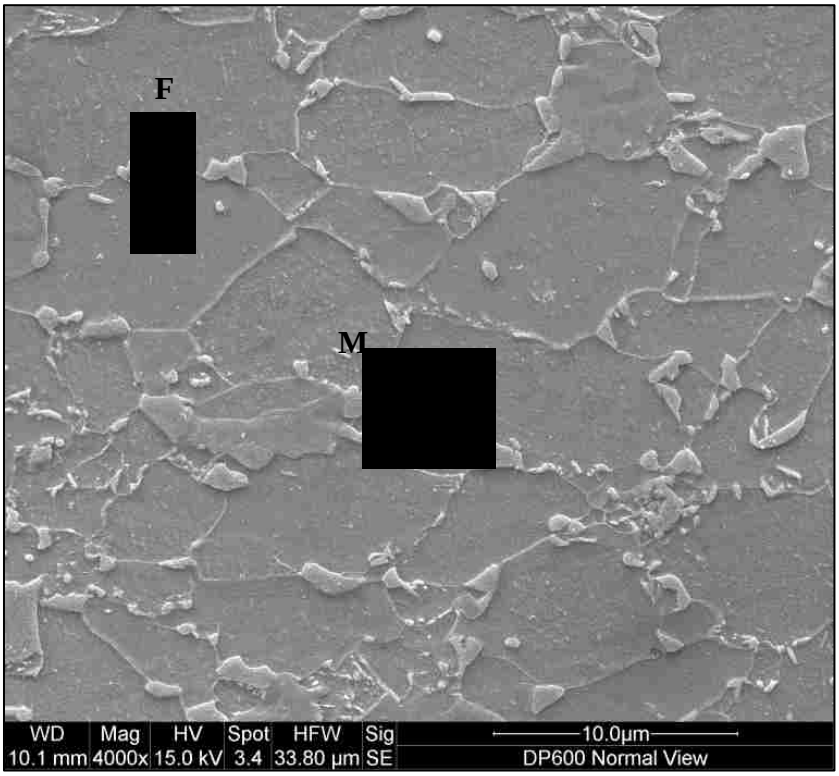

Figure 2.1: Dual phase microstructure. F = ferrite; M = martensite

2.1.1 Processing of Dual Phase Steels

Two methods are commonly employed to create a DP microstructure: sequential quenching and intercritical annealing. Prior to the intercritical or sequential quenching heat treatments, the low carbon steel is cast into a billet, hot rolled, and put through a series of cold rolling operations to reduce it to a final sheet thickness.

In the sequential quenching process, the steel is heated to the austenite region of the iron-carbon phase diagram and held there to effect a fully austenitic microstructure. The steel is then cooled to the ferrite + austenite region and held at that temperature to allow the nucleation of ferrite at the austenite boundaries. After nucleation, the ferrite grows into the austenite grains. At this stage, a uniform temperature must be achieved across the entire steel sheet to ensure a mixed ferrite and austenite microstructure even at the centre. The steel is then quenched to room temperature to form blocky martensite from the austenite in the ferrite matrix. Depending on the carbon content in the austenite prior to quenching, the martensite will form either laths or plates [4, 5]. The sequential quenching process is used primarily for wheels, bumpers, and suspension components [6].

The intercritical annealing process, Figure 2.2, is generally used for thinner sheets, such as those for automotive body components. The starting microstructure of the sheet is a ferrite-pearlite mix that has been cold rolled to the desired thickness. The sheet is heated into the ferrite-austenite region of the iron-carbon phase diagram, where the pearlite dissolution occurs. This reaction is often too rapid to study in depth [7]. Depending on the annealing temperature, pearlite dissolution is believed to take from fifteen seconds to

two minutes in most low-carbon steels. If annealing occurs for longer than required for pearlite dissolution, the austenite volume percentage will continue to increase for up to twenty-four hours [7]. Unlike austenite, ferrite grain size does not vary significantly with intercritical annealing time [8].

Austenite nucleates and grows along the ferrite grain boundaries and into the ferrite grains to reach equilibrium at the annealing temperature. Increasing the intercritical annealing temperature increases the amount of austenite in the microstructure, which in turn lowers both the carbon content of the austenite, as well as the hardenability of the steel. These factors are associated with decreasing amounts of retained austenite [8]. As diffusion continues through austenite grains, carbon concentration gradients are eliminated. Once there are no more concentration gradients, austenite equilibration ceases. Intercritical annealing is a slow process; as a result, diffusion is not completely finished [7].

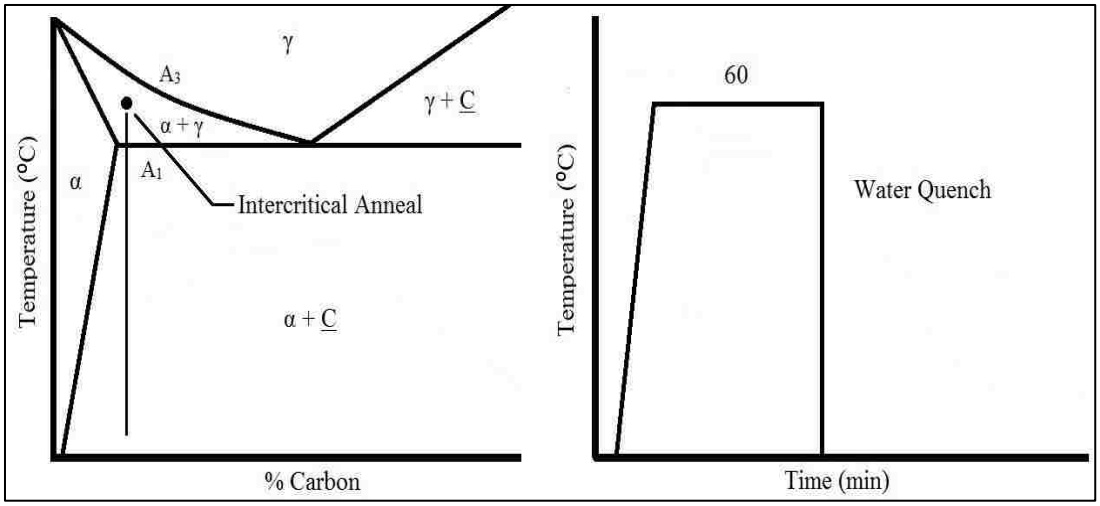

Figure 2.2: Intercritical annealing of DP steel

The austenite grains in the steel transform to martensite upon quenching following the intercritical anneal and form phase islands in the ferrite matrix. The locations of the non-ferritic phase islands after the intercritical annealing heat treatment are dependent on the condition of the material before intercritical annealing. If the microstructure has been quenched and tempered or cold rolled, the non-ferritic phase islands will be determined by the size and distribution of the pearlite colonies and carbides prior to annealing [8].

In some cases, there will be retained austenite in the quenched microstructure. Retained austenite commonly exists at the edges of martensite islands due to some austenite reverting to ferrite during cooling. Ferrite rejects carbon into the austenite as it cools, which lowers the local martensite finish temperature to below room temperature [8]. Islands of second phase particles smaller than 1 μm remain as retained austenite [9]. The soft matrix experiences localized yielding around these non-transformed particles and therefore the strain is not communicated to activate the martensite transformation [8].

If the microstructure has been spheroidized prior to annealing, the austenite will grow at carbide sites preferentially at the ferrite grain boundaries and will quench to martensite islands at those locations. The greatest increase in volume percent of non-ferritic phase islands in the microstructure is seen with a starting microstructure that has been cold rolled or quenched and tempered, as well as the largest possible martensite island size [10].

Comparing the two processes, in the intercritical annealing process austenite nucleates and grows at ferrite grain boundaries; in sequential quenching, ferrite nucleates and grows at the austenite grain boundaries. The annealing time (holding time), along with the temperature and cooling rate, determine the volume fraction and composition of phases in the final microstructure. At higher annealing temperatures, the carbon content decreases in the austenite; but the volume fraction of austenite itself will increase. The amount of martensite formed by quenching is a direct result of the amount of austenite in the microstructure, but is also affected by the presence of elements such as carbon, manganese, and silicon.

A third, less common method of producing DP steels is intermediate quenching. In this process, the steel is heated to the austenitic region and held for about thirty minutes to ensure that the structure consists of only austenite. It is then water quenched to room temperature, which forms a fully martensitic microstructure. The sample is then heated for approximately sixty minutes in the ferritic/austenitic region to form ferrite at the grain boundaries. Finally, it is quenched to transform the austenite back into martensite islands to finalize the DP structure [11]. This process is associated DP steel with higher martensite content used in mineral and mining parts which do not require welding operations.

2.1.2 Effects of Alloying Elements in DP Steels

In general, alloying elements increase the strength of steel. For DP steels, a particular concern is their effect on hardenability. Since DP steels are created using low carbon

steels, the alloying elements are also responsible for increasing hardenability in the steel. The elements most commonly added to DP steels are: manganese, molybdenum, chromium, and silicon.

Alloying elements also affect the transformation behaviour of the steel. The shape of a time temperature transformation (TTT) curve for steel, Figure 2.3, will shift depending on the elements added. The martensite, bainite, or pearlite start temperatures, and the amount of time required to hold until formation is complete can be affected by alloying.

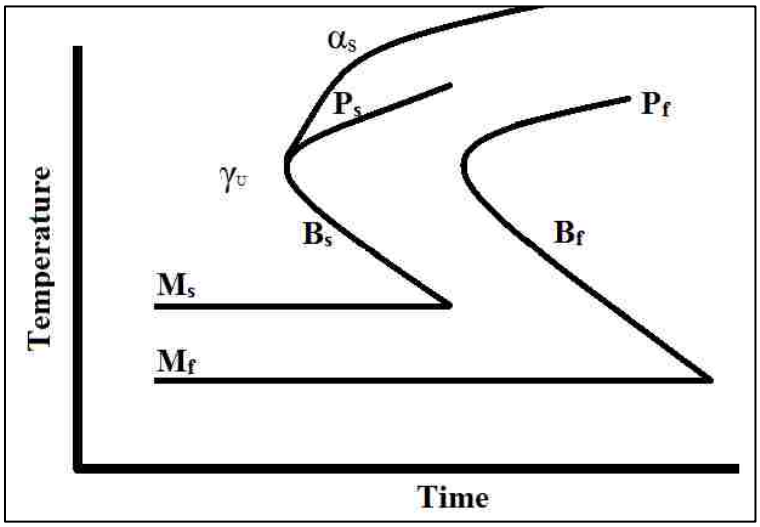

Figure 2.3: General TTT curve for steel

A common alloying element in steels is manganese, which acts as an austenite stabilizer. Manganese diffuses into ferrite due to its low diffusivity in austenite, and with shorter holding times in the intercritical annealing process, manganese is trapped at the edges of austenite grains. This effect provides an increase in local hardenability, allowing martensite formation at the edges of the grains. Manganese also decreases the activity of carbon in austenite, which allows martensite to form at slower cooling rates [12]. Manganese also plays a role in banding, which is discussed below in section 2.1.3.

Molybdenum also increases the hardenability of steel, which allows martensite to form at slower cooling rates. It also stabilizes cementite (Fe_3C), which necessitates longer annealing times to dissolve the carbides [13]. Additionally, it promotes bainite formation due to its slow diffusion in pearlite, which delays the P_s time.

Chromium is a ferrite stabilizer which acts to decrease the extent of the austenite phase field. It partitions between ferrite and cementite in the microstructure depending on carbon content [6]. Much like molybdenum, it also allows martensite to form at slower cooling rates while stabilizing cementite. Additions of chromium also affect the bainite region of the phase diagram, causing it to expand [13].

Silicon increases carbon diffusion into austenite in the microstructure. It also retards the formation of cementite and, as a result, pearlite. It acts as a solid solution strengthener and increases the strain hardening rate of DP steels [14].

Vanadium and titanium shrink the austenite phase field in the iron-carbon phase diagram. They are also prone to forming carbides and carbonitrides. These precipitates contribute to strain hardening as obstacles for dislocation motion within the ferrite, thus increasing the yield strength of the steel [15].

Additions of niobium to the microstructure are used to refine the grain size in the steel. Niobium causes second-phase particles, which pin the grain boundaries. It is the main

mechanism for controlling the grain size. Grain size refinement allows control of the strength and ductility characteristics of the steel to an extent, as increasing grain size leads to lower strength and higher ductility [4].

2.1.3 Banding

Banding is a phenomenon in metals that takes place due to segregation of substitutional alloying elements during solidification. The elements that are most commonly associated with segregation are manganese, chromium, and molybdenum. They affect the solidification temperature range of the steel melt. The dendrites formed in the solidification process are typically lower in alloy content; the interdendritic spaces are enriched in alloy content. During rolling processes, these interdendritic spaces are elongated into parallel bands [16, 17]. The distribution of the alloying elements in the bands introduces an additional source of anisotropy in the finished sheet. Quantification of banding is difficult; as such, the level of banding in sheet materials is typically done qualitatively through comparison [18].

There are differences in austenitic transformation behaviour in these bands. Uneven distribution of carbon and other elements causes layers of martensite, bainite, ferrite, and pearlite to form. Manganese is found to be mostly responsible for the difference in austenite transformation behaviour. Carbon diffuses from areas with low manganese to high-manganese areas due to the ferritic allotriomorphs rejecting it. This carbon migration causes changes in the A_{e3} temperature within the bands. Carbon enrichment in

the high-manganese areas creates regions of low A_{e3} temperature. As such, the local percentage of austenite is increased [16, 17].

Banding is also affected by the cooling rate, austenite grain size, and austenitizing temperature. Banding increases with decreasing solidification rate; therefore, a faster solidification rate will suppress the effect of banding in the microstructure. Band thickness strongly impacts the continuous cooling transformation (CCT) behaviour of the local microstructure. Thicker bands correspond to an increase in hardenability of the microstructure, but the time to complete the austenite-to-martensite transformation is extended due to a lower martensite finish temperature [16].

It is known that microstructural banding is induced in the microstructure prior to intercritical annealing, specifically during casting and rolling operations. High temperature treatment performed over time on the sheet after banding has set in fully removes the banding from the microstructure. High temperature homogenization treatments can remove underlying compositional gradients, but this process is not feasible in an industrial situation, because it requires significant time for the diffusion of substitutional elements to take place [16, 17].

2.1.4 Structure-Property Relationships

The general relationship found by Fischmeister and Karlsson [19] states that, if the Young's moduli of both constituents are approximately equal, the yield strength of the soft matrix for DP steels will govern the initiation of plastic deformation. Any variation

of the overall yield strength with cooling rate/martensite volume fraction should be attributed to a change in yield strength of the ferrite matrix. This change in yield strength is believed to be due to the austenite to martensite transformation.

The austenite to martensite transformation is a diffusionless process with no significant change in atom positions. The transformation alters the crystal structure of the face-centred cubic (FCC) austenite. The lattice transformation is dependent on carbon content: if the carbon content is less than 0.2 wt%, the austenite will transform to a body-centred cubic (BCC) structure matching that of α ferrite [6]. Higher carbon contents will cause the horizontal axis to shrink slightly and the vertical axis to grow noticeably with carbon above about 0.2 wt%; thus the lattice distorts to a body-centred tetragonal structure (BCT) [6, 20]. The transformation from austenite to martensite creates a tensile residual stress in the microstructure [21].

The degree to which the cell volume changes will impact the matrix via the stress imposed and the dislocations created [20]. Dislocations are imperfections in a crystal structure that disturb the local arrangement of atoms. These imperfections, or defects, can affect the properties of the structures that contain them [22]. The austenite to martensite transformation causes a dislocation network that partially links martensite islands, which contributes to the initial deformation process [21]. Dislocation tangles form in ferrite near martensite and retained austenite particles. Stress on the material relaxes the build-up and allows dislocation motion, which promotes continuous yielding [8, 23]. The flow stress in the steel is proportional to the square root of the total dislocation density in the martensite

and the ferrite. The dislocation density depends on the harder phase in the microstructure, predominantly martensite [21].

The morphology of martensite affects the deformation process as well. If the martensite grains are elongated and larger, they are often distributed along the ferrite grain boundaries. This distribution pins the boundaries and prevents the flow of ferrite grains, which in turn initiates the brittle cracking mechanism of failure [12]. Equiaxed martensite grains contribute to increasing the uniform strain of the material. The fracture stress of DP steel increases with equiaxed martensite compared to the banded structure for steels that contain a volume fraction of less than fifty percent martensite [24].

An increase in the volume fraction of martensite in the microstructure of DP steel increases the true fracture stress and strain of the material; this results in an increase of the tensile strength, the work hardening rate, and the hardness of the metal [7, 8, 15, 21, 23]. A higher martensite volume fraction causes martensite islands to constrain the ferrite more compared to steel with a lower martensite volume fraction. As such, it leads to a lower ferrite contribution to the stress on the microstructure. A lower martensite volume fraction combined with a higher carbon content in the ferrite results in less deformation of the martensite islands [25].

To optimize the microstructure for the best strength and formability combined, a fine distribution of martensite in a ferrite matrix with a small grain size is desired [15]. The finer dispersion increases the ductility of the steel [23]. Finer dispersions can be achieved

through nitrogen additions to the steel [8]. At a given martensite volume fraction, a decrease in martensite particle size will increase both the work hardening rate and the maximum elongation, while the tensile strength will remain unaffected [8, 9]. At low strain values, the strain hardening rate will increase with a smaller ferrite grain size. As stated in section 2.1.2, one way to manage grain size is through alloying content with elements such as niobium.

The need for a small grain size is explained by the Hall-Petch relationship, Equation 2.1.

$$\boldsymbol{\sigma_y = \sigma_o + \frac{k_y}{\sqrt{d}}} \tag{2.1}$$

where σ_y is the yield stress of the material (MPa), σ_o is a material constant known as the starting stress for dislocation movement (MPa), k_y is a material constant known as the strengthening coefficient (MPa $m^{1/2}$), and d is the mean grain diameter (μm) [26].

A steel with a smaller grain size has more grain boundaries, which interrupt dislocation motion. The dislocations pile up and create stress concentrations. As such, smaller grain sizes increase the yield strength of a material [26]. Although this mechanism improves the yield strength, work hardening is the principal means of increasing yield strength in DP steel and is described below in Section 2.1.5.

DP steels may contain small amounts of bainite in addition to martensite as a result of the heat treatment process. The austenite to bainite transformation creates dislocations similar to the austenite to martensite transformation; however, the bainite transformation creates fewer dislocations. The lower number of dislocations means the initial mobile

dislocation density is lower in areas with bainite compared to those with martensite. The presence of bainite in DP steel also improves yield strength and ductility [23].

The strength of dual phase steel depends on the relative amount of martensite, ferrite, and bainite and their respective strengths, which depend on carbon content. In other words, the internal stresses of the phases and constituents of dual phase steel ultimately govern the overall internal stress of the steel [23].

2.1.5 Work Hardening

Work hardening is due to dislocation density and long range stress. Some dislocations are necessary to accommodate strain gradients caused by phases with different plasticities, while others are stored from deformation [8]. The austenite to martensite transformation creates dislocations that are able to flow through ferrite and pin on martensite islands as stated in the previous section. As the dislocations pile up, the work hardening process occurs. With each successive deformation, the dislocations pile up more to resist further deformation [23, 27].

In dual phase steels, a higher martensite volume fraction corresponds to a higher initial dislocation density due to the number of dislocations created in the austenite to martensite transformation [21, 23]. A higher initial dislocation density results in a rapidly decreasing value of the work hardening exponent. The work hardening exponent, n, has a value between 0 and 1; 0 corresponds to a perfectly plastic material, and 1 to a perfectly elastic material [27]. It is the exponent of the power law function in Equation 2.2:

$$\boldsymbol{\sigma = K\varepsilon^{n}} \quad (2.2)$$

where σ is stress (MPa), K is a material constant known as the strength coefficient (MPa), ε is strain (mm/mm), and n is the work hardening exponent (unitless) [27].

The decrease in the work hardening exponent is due to localized plastic strain in ferrite, the extent of which is determined by the average density, distribution, and mobility of the dislocations, as well as the associated ferrite strain [23].

The process of work hardening in DP steel occurs in three stages:

1. First, the glide of mobile dislocations near martensite particles allows homogeneous deformation in the ferrite matrix.
2. The rate of work hardening diminishes due to constrained ferrite deformation in the presence of the rigid martensite.
3. Finally, dislocations pile up at the ferrite/martensite interface and martensite may experience plasticity. Ferrite and martensite grains then deform simultaneously [23, 28, 29].

2.1.6 Deformation and Fracture Characteristics

Due to the nature of the microstructure, the manner in which DP steel fails is dependent on the fraction of phases present and the amount of strain applied to the microstructure. If the martensite volume fraction is low, fracture demonstrates a more ductile mode [30]. Slip bands form in ferrite early in the deformation process and propagate through the matrix to towards martensite islands. These slip lines occur at a 45° angle to the load axis

[25]. In steels with high martensite volume fraction, the slip lines bypass the martensite islands like waves, Figure 2.4. The martensite islands do not visibly deform at strain up to necking, but at higher plastic strains in the necked portion of a specimen the martensite particles align parallel to the elongation [31].

Stress is transferred along ferrite boundaries to the martensite islands proportional to the area of the interface, shear stress in the matrix, and an orientation factor, γ [31]. The driving force of the stress transfer is the strain gradient between the two phases that exists due to the fact that dislocations in ferrite grains near martensite islands exist to relieve the initial tensile residual stress [21]. The dislocation motion allows deformation in ferrite to occur faster and earlier in the process because of the incompatibility at the interface caused by martensite remaining elastic in the early stages of strain. This dislocation density gradient in the ferrite grains increases closer to the martensite/ferrite interface. The natural stress concentrations between the phases yield inhomogeneous deformation [21] and cause shearing along the martensite/ferrite interfaces, which causes the martensite islands to deform after necking begins [25].

Figure 2.4: Slip lines bypassing martensite islands [25]

Strain in martensite and ferrite increases approximately linearly with macroscopic strain. With constant carbon content, the difference between martensite and ferrite strains increases with increasing martensite volume fraction. With constant martensite volume fraction, the difference in strains between the two phases increases with lower carbon content [25]. The plastic deformation of martensite is dependent on carbon content; with high carbon content in martensite, no plastic deformation occurs in martensite [21]. The uniformity between the two phases can be represented by a strain ratio, R, which is equal to the strain in martensite divided by the strain in ferrite. R increases with either increasing martensite volume fraction or decreasing carbon content.

At low strain rates, dislocations move and build up, leading to catastrophic failure due to yielding in multiple locations in the microstructure [15]. As stated above, the microstructure begins to deform close to martensite islands in the early stages, which initiates a high rate of dislocation creation. As strain increases, deformation moves towards the centre of the ferrite grains. Undeformed ferrite can be considered hard and approximated to be similar to martensite; therefore, a stress concentration may arise between the deformed and undeformed ferrite. The stress concentration begins the process of void nucleation and growth in ferrite, which retards the rate of dislocation creation in ferrite grains [21]. The random nature of the dislocations and martensite island locations dictates that plastic deformation may not occur simultaneously within and among ferrite grains [31]. Not all ferrite will be deformed when necking occurs; the amount of undeformed ferrite increases with the martensite volume fraction [21].

Increasing martensite volume fraction leads to an increase in the work hardening rate, which delays the growth of voids [8].

Early in deformation, voids nucleate and grow at inclusions in ferrite and at ferrite boundaries. This leads to decohesion between softer ferrite and harder particles [31]. Larger than average size particles at ferrite grain boundaries are the most common site for voids, which grow with increasing strain [31]. Failure occurs when the voids at the grain boundaries grow and coalesce parallel to the applied load. The main causes of void nucleation are martensite cracking and separation, and decohesion of the ferrite-martensite interfaces with increased strain [30]. Decohesion at the ferrite/martensite boundaries occurs at approximately 0.5 strain in the microstructure [8].

In the case of martensite cracking, microcracks initiate in the martensite islands and propagate perpendicular to the applied load, ending at the softer ferrite matrix [12]. After reaching the ferrite matrix, they eventually cause quasi-cleavage fracture in the ferrite grains [23]. These cracks form voids that lead to coalescence and ultimately brittle failure at the edges of the fracture surface; this type of failure typically exhibits shallow cusps across the fracture surface [12]. This brittle type of fracture is more common at high martensite volume fractions. The fracture surfaces show minimal plastic deformation before failure and the cause of fracture is the formation of microcracks perpendicular to the tensile axis [30].

2.2 Sheet Metal Forming

2.2.1 Die Forming

Traditional sheet metal forming methods typically employ two mating tools to shape sheet steel. Stamping with rigid tooling uses a punch, a female die, and a blank holder [32, 33]. A simple example of this is a stretch-form test for formability studies, such as the Nakazima test. In this test, a sheet metal blank is stretched over a hemispherical punch to failure [34]. In stamping operations, there is friction on both sides of the sheet which contributes to a reduction in formability. Higher hardness materials inherently have lower formability, but they also increase the wear on the tools and shorten their service life [33].

2.2.2 Hydroforming

Hydroforming is a modification of traditional forming or stamping where either the punch or die is replaced with a cavity filled with fluid, usually oil or water. In other words, the fluid can be used as a punch, draw die, or as a method of assisting a forming process [35, 36].

In the case of hydromechanical deep drawing, Figure 2.5, a punch forces a sheet metal blank into a cavity filled with fluid; the pressure from the fluid forces the sheet onto the punch as material is drawn in. Fluid lubrication reduces the frictional force on the side of the sheet in contact with the fluid. The reduction of friction and the high fluid pressure allow common stamping materials to be used in hydroforming to achieve higher formability [37-40]. The replacement of die contact with fluid contact on one side of the part results in a higher quality surface appearance as well [37].

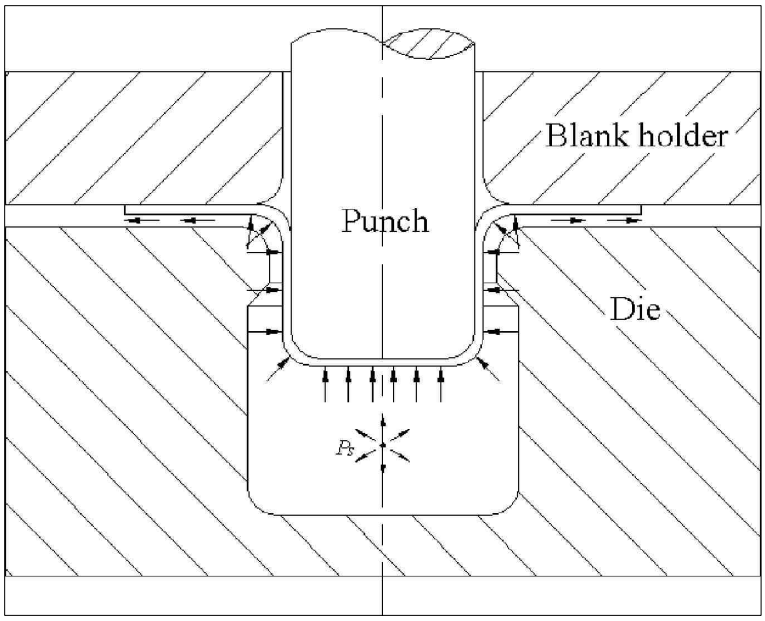

Figure 2.5: Hydromechanical Deep Drawing [36]

2.2.3 High Strain Rate Forming

Several researchers [41-51] have reported increased formability of higher strength, lower ductility materials using high strain rate forming processes. There are various high strain rate forming processes in use, but the three that will be discussed here are explosive forming, electromagnetic forming, and electrohydraulic forming.

Explosive forming has been in use since the nineteenth century [52]. In modern operations, there are a few essential components to explosive forming. The first is the transfer medium in which the explosive is placed, most commonly water for cost and the effectiveness of shock wave propagation. For sheet forming, the explosives are submerged in the water above the blank. High explosives are most commonly used, as the pressure resulting from detonation is much greater than that generated by low explosives such as cordite. A small portion of the generated energy is directed toward the blank and die, which are positioned below the explosives, Figure 2.7, and the piece is formed as a

result. Air is evacuated from between the sheet and the die to remove air resistance to the sheet travel.

The advantages of explosive forming are: the reduction of cost with less equipment; fewer welds required; and precise tolerances. The disadvantages are: consumable explosives required; large amount of water required for each operation; long cycle times; and low volume production [52].

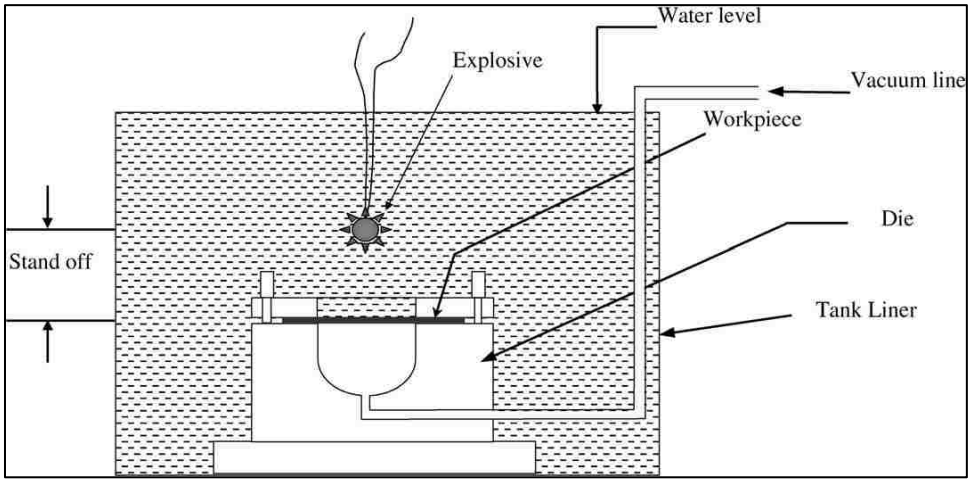

Figure 2.6: Explosive forming of sheet metal [52]

The electromagnetic forming (EMF) process is shown schematically in Figure 2.8. A large capacitor bank stores energy that is discharged at high voltage through a coil or electromagnetic actuator in the proximity of the workpiece [44]. The discharge produces a strong transient magnetic field that induces eddy currents in the conductive workpiece or driver. The eddy currents produce a secondary magnetic field around the workpiece, which causes the workpiece and the coil to repel one another through a Lorentz force. At constant launch energy, a thinner, lighter workpiece will experience a higher impact velocity. Sheet impact velocity has been reported at 100 m/s with strains in the range of

30-50%. It was found that the sheet boundary conditions, such as punch geometry and launch velocity, have a greater effect on formability than the reported quasi-static ductility [41]. Imbert et al. [53] modeled EMF of aluminum sheet and estimated strain rates at the time of die impact ranging from 30,000 to 69,000 s^{-1}. It was proposed that the inertial and through-thickness compressive and shear stresses, as well as the non-linear strain paths, were responsible for improved formability at this range of strain rates.

The advantages of EMF are: lower tooling cost; improved formability with higher velocity; and better surface finish on one side of the workpiece. Some disadvantages are: the need for a driver plate in non-conductive materials; and safety considerations with the high energy required.

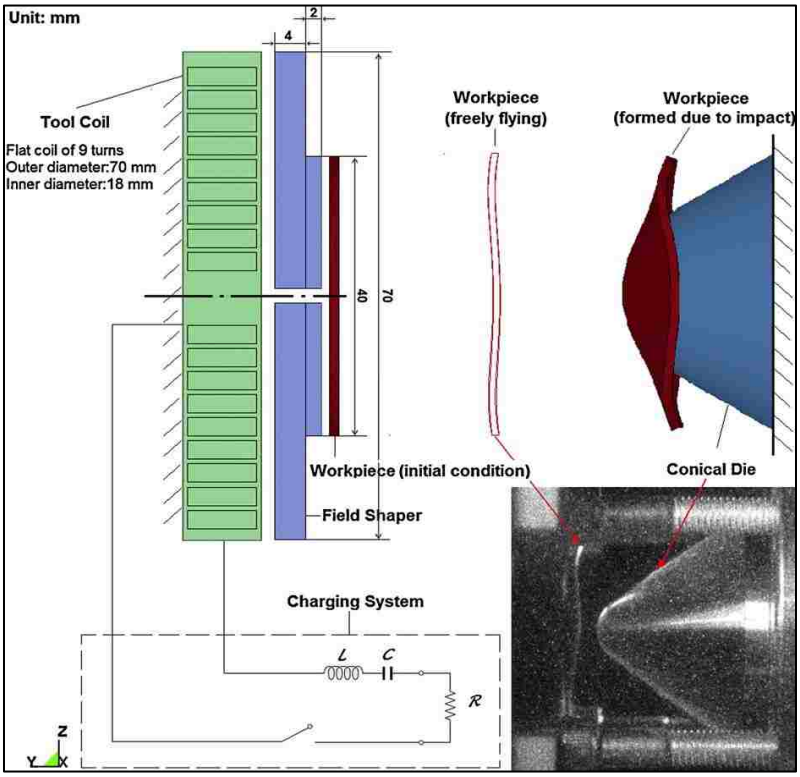

Figure 2.7: EMF setup [54]

2.2.4 Electrohydraulic Forming

High strain rate experiments using electrical discharge in water were conducted as early as the eighteenth century, notably by Lane (1767) and Priestly (1769) [51]. The process of electrohydraulic forming (EHF) takes advantage of an explosive shockwave in water to form a sheet metal blank in approximately 1 ms, Figure 2.9. EHF can be executed with a die, called electrohydraulic die-forming (EHDF), or without a mating die, called electrohydraulic free-forming (EHFF). Compared to traditional forming methods, such as stamping and hydroforming, the cost of EHF is much lower than stamping in terms of the amount of tooling required: only one die and no punch or large press is required [55].

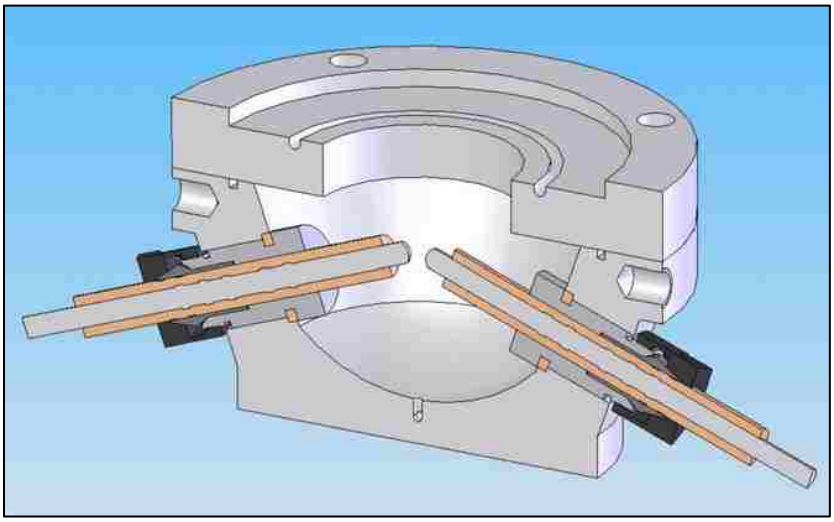

Figure 2.8: EHF chamber with electrodes, half section [51]

A capacitor bank stores energy and discharges it at high voltage across two submerged electrodes [51, 52]. The two electrodes face each other horizontally and are connected by a wire known as the “bridge wire” in order to improve the consistency of the pulse. They are positioned in a cavity filled with water with the sheet metal acting as one wall in the chamber [55]. The high voltage creates a high pressure, high temperature plasma channel

between the electrodes. At the start of the discharge, the plasma channel resistance drops and the current grows rapidly [51]. A shockwave is subsequently initiated by the expansion of the channel. The mass and momentum of the water in the shockwave forms the sheet metal into the die above [2]. The volume of air between the blank and the die is evacuated by means of a vacuum pump during setup prior to discharge in order to reduce the air resistance to blank travel and improve formability [51, 55]. The relative position of electrodes can help to focus and optimize the shockwaves for formability [42, 43].

There are multiple variables and issues associated with EHF. The energy stored in the capacitor bank dissipates somewhat before reaching the electrodes to create a spark, and the existing time delay before the spark breakdown determines how much of that energy is dissipated [2]. Another factor in the discharge initiation time is the time for the bridge wire to melt during the process [41].

The deformation of the blank is due to the shockwaves in the fluid travelling to the blank as opposed to the expansion of the gas due to the discharge. The blank begins to deform with the arrival of the resulting shock waves, and the gas bubble arrives after, continuing to expand after the blank is formed [43]. The velocity-time plot of the sheet centre of EHF, Figure 2.9a), reveals two maxima in the profile of both free- and conical die-forming conditions. The two maxima correspond with the expansion of the plasma channel and gas bubble, as well as the reflection of the pressure wave off of the moving sheet. The resulting collapse of the bubble in the water through the discharge process is observed after the second maximum as the fluctuations in velocity shown in the plot [46,

56]. Away from the centre of the sheet, however, the velocity-time profile displays a single-peak form similar to what is observed in EMF trials across the whole sheet [45, 57, 58].

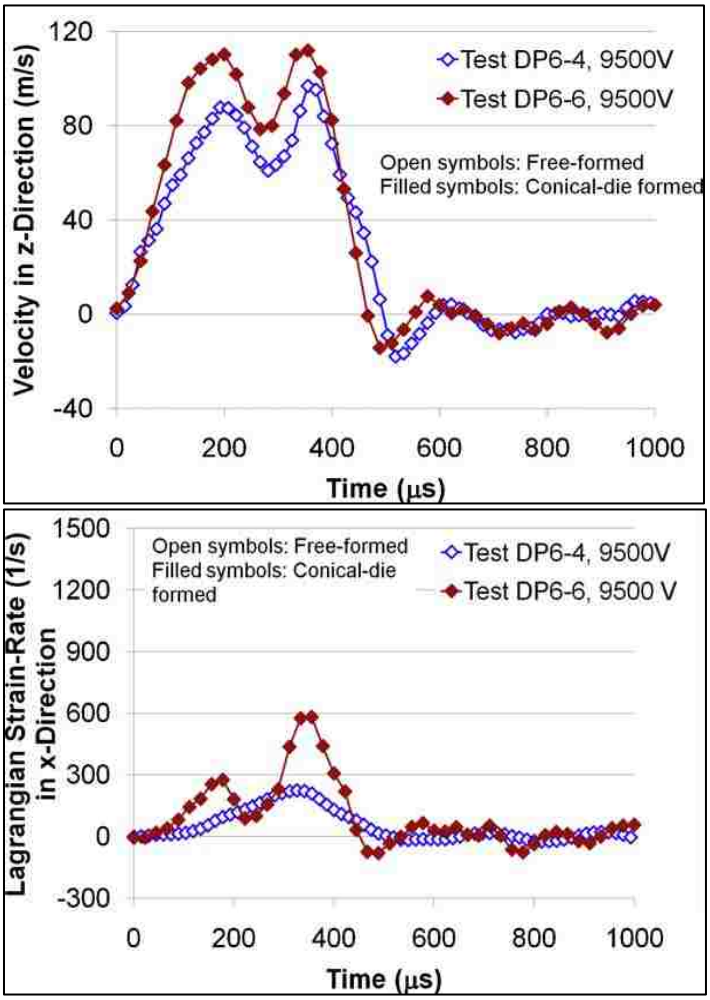

Figure 2.9: a) Velocity-Time profile and b) Strain Rate-Time profile for EHF of DP600, EHDF and EHFF [46]

A common configuration is EHDF with a conical die [47, 48], Figure 2.10, for exploring a nearly equi-biaxial strain path [46]. Deviation from an equi-biaxial strain path is believed to be due to the interaction of the pressure pulse with the die, as well as non-symmetrical friction conditions at the sheet/die interface at the apex of the conical die [46].

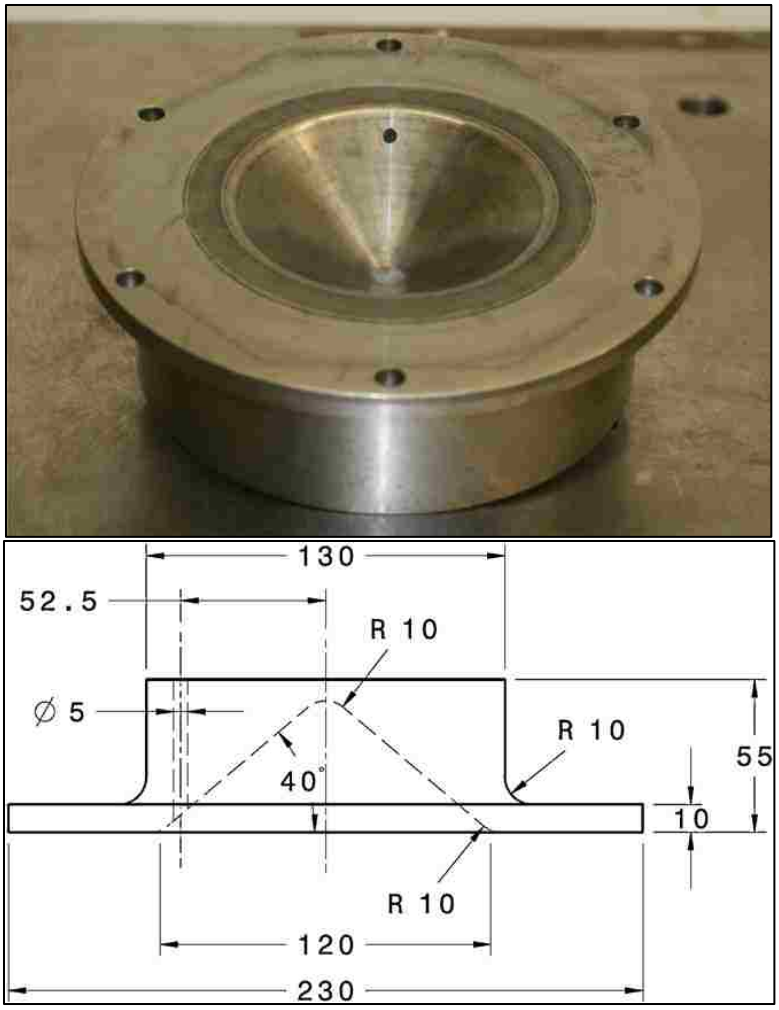

Figure 2.10: Conical die for electrohydraulic die forming, units are mm [51]

At the end of the velocity-time profile, there is a fluctuation between positive and negative velocities that indicates reverberation in the sheet, in both free- and die-forming [46]. The velocity in EHDF was greater than EHFF for all cases in this study, which could be explained by the interaction of the sheet with the die during forming. As the sheet progressively forms against the die wall, the remaining unformed area of the sheet decreases and benefits from all of the remaining kinetic energy [45].

As the voltage of the discharge is increased, the input energy increases; higher energy leads to an increase of velocity and strain rate in the moving sheet. The resulting profile of the strain rate-time plot is similar to the velocity-time plot, showing two maxima. The strain rate maxima occur earlier in the process than the maxima in the velocity plot, Figure 2.9 [46]. The peak values of strain rate vs time at the centre of the sheet in conical die forming are due to the extrusion force of the forming process and high velocity. The resulting strain values are higher slightly away from the centre due to frictional forces between the sheet and die [59]. The negative strain rate at the end of the process is due to elastic unloading of the metal [46].

The strain rate in EHDF is higher than in EHFF, similar to the velocity plot, Figure 2.11a. The strain rate in EHFF shows a gradual rise and fall, whereas the strain rate in EHDF follows the same mechanism of strain rate amplification due to the focusing effect of the conical die. This focusing effect in the conical die is more effective in increasing strain rate than the increase in voltage alone, and results in greater final strain values as well [46].

The deformation mechanisms of DP steel are strain rate-dependent. In EHF, there is a progression of strain-rate depending on the point in time in the process and the location on the blank. Figure 2.11 shows predictions of such behaviour [60]. When the blank is deforming in EHF, there is a speed gradient across the sheet, which creates inertial stabilization effects in the blank. Inertial stabilization is the diffusion of deformation

through the specimen at high velocity, which stabilizes the material against necking [41, 42, 48].

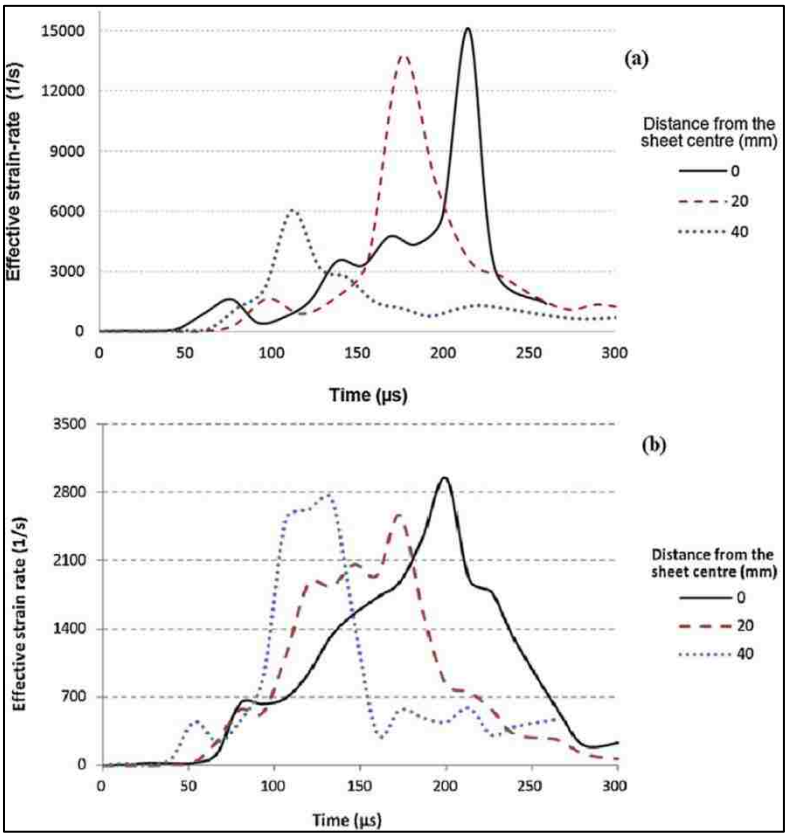

Figure 2.11: Predicted history of effective strain rate; a) EHDF, and b) EHFF [60]

In addition to the inertial stabilization, improved formability is achieved through the high strain rate and high rate of impact with the die, which creates through-thickness compressive stresses [41, 50, 61, 62]. These stresses can be seen in Figure 2.12 for two cases of EHDF simulations with input energies of 14.4 kJ and 19.3 kJ. In the first case, it should be noted that the minimum principal stress is greater 20 mm away from the centre of the sheet than at the centre, where the apex of the specimen is located. In the second case, the apex showed the highest minimum principal stress. In both cases, the edge (40 mm from centre) showed the lowest absolute value of stress.

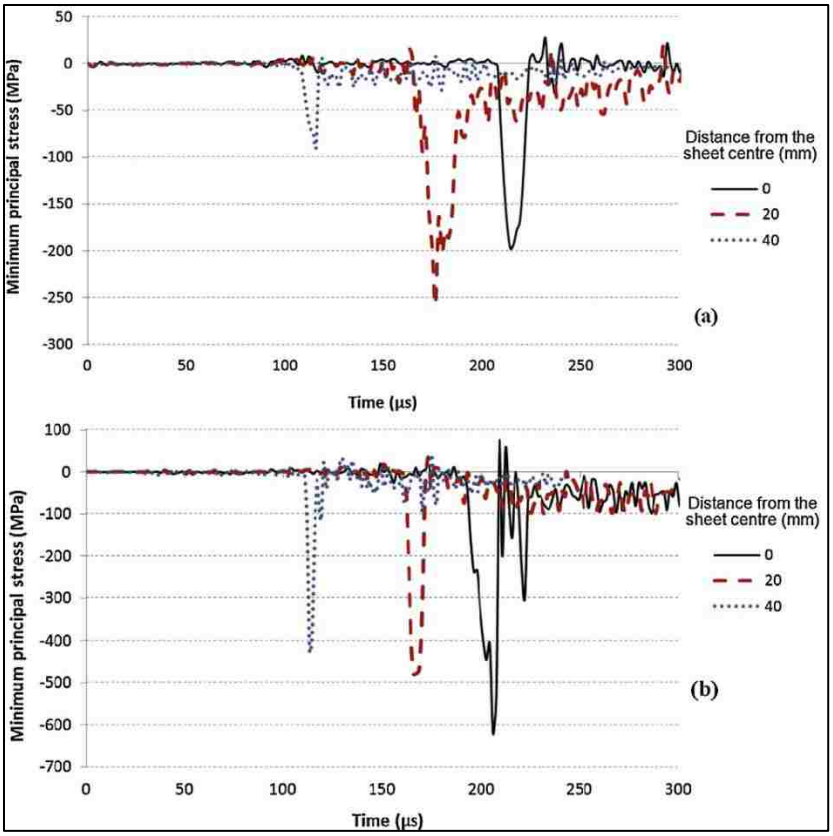

Figure 2.12: Minimum principal stress history in two EHDF cases: a) 14.4 kJ; and b) 19.3 kJ [60]

As described in Section 2.1.6, DP steel fails by a mechanism of void nucleation and growth. These mechanisms are also active in high strain rate forming such as EHF [63]. The progression of void volume fraction with increasing strain in the microstructure of DP steel follows an exponential trend, Figure 2.13.

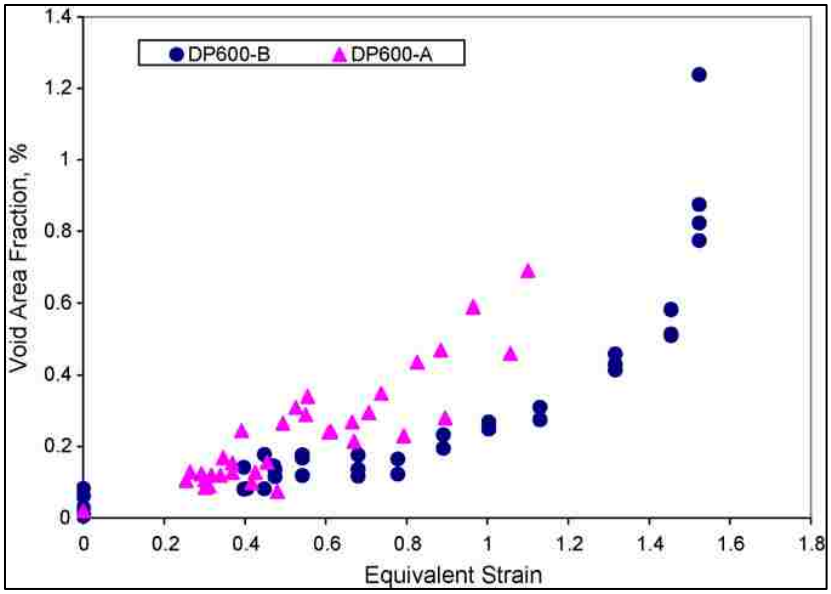

Figure 2.13: Void Volume fraction vs Equivalent Strain plot [63]

2.3 Summary of Literature

The following are the key concepts that relate directly to the current research. They will be referenced in the discussion.

- The microstructure of DP steel is comprised of a soft, ductile annealed ferrite matrix and hard martensite islands at grain boundaries formed by intercritical annealing.
- The austenite to martensite transformation creates dislocations in the surrounding ferrite. The ductile deformation mechanism of the steel is the dislocation motion through ferrite. The dislocations glide until they pin on martensite islands; the pileups of dislocations successively build up resistance to further dislocation motion and cause a work hardening phenomenon.
- At low strains in the microstructure, the presence of shear at the ferrite/martensite interface causes microcracks in the martensite, which lead to voids and quasi-cleavage cracking through the softer ferrite surrounding the martensite island. At increased strain, the ferrite deforms while the martensite remains elastic. At

approximately 0.5 strain, decohesion occurs between the two phases, which nucleates voids that grow and coalesce into cracks.

- The Nakazima test is a quasi-static forming test that stretches a sheet metal blank over a hemispherical punch to failure, with a strain-rate of 10^{-3}-10^{-1} s^{-1}.
- Electrohydraulic forming (EHF) involves a high voltage discharge across two electrodes in a water chamber that create a shockwave, which propagates to the surface to cause a sheet metal blank to deform. If no mating die is used, this is called free-forming (EHFF); if a die is used, it is called die-forming (EHDF). The strain rates in EHDF can peak in the range of 10^4 s^{-1}.
- EHDF using a conical die experiences higher peak strain rates ($1.5x10^4$ s^{-1}) than EHFF ($3x10^3$ s^{-1}). The through-thickness compressive and shear stresses generated by die impact in EHDF improve the formability of the steel by delaying void growth.

Chapter 3 :

Experimental Procedures

3.1 Materials

This research investigated the low and high strain rate behaviour of DP600. 1.5 mm steel sheet was provided in the cold rolled condition by ArcelorMittal Dofasco. Table 3.1 lists the chemical composition of this steel.

Grade	C	Mn	Mo	Si	V	Cr	Ni	Cu	Al
DP600	0.107	1.497	0.214	0.175	0.044	0.181	0.015	0.057	0.038

Table 3.1: Chemical composition of DP600

ASTM standard A1088-13 details requirements for grades of DP steel, which are listed in Table 3.2. The DP600 for the current work is shown in the table and meets all requirements according to the standard.

Grade	Maximum Content			Minimum Requirements		
	%C	%Mn+Al+Si	%Cr+Mo	YS (MPa)	UTS (MPa)	%EL
DP490	0.15	3.4	1	290	490	25
DP590	0.17	4.75	1.4	340	590	21
DP780	0.18	5.4	1.4	420	780	14
DP980	0.23	6	1.4	550	980	8
ArcelorMittal DP600						
DP600	0.107	1.71	0.395	380	619	25.1

Table 3.2: ASTM A1088-13 requirements for DP steels [64]

3.2 Electro-Etching Grids

Prior to Nakazima, EHFF, and EHDF testing, 20 cm x 20 cm blanks were electro-etched with square and circle grids for strain measurement. The power source was set to AC current with the interpolation setting on, and the voltage dial set to 19 volts. A sacrificial metal sheet of DP600 was cleaned with acetone, dried, and connected to the positive side of the power supply. The following components of the electro-etching process were layered on top of the sacrificial sheet as noted in Figure 3.1, in order: the blank to be gridded, the stencil, and the felt wick.

With the power supply turned on and the metal roller connected to the negative terminal, the roller was slowly rolled over the blank to etch the grid on the surface. After the rolling was complete, the power supply was turned off, and the wick and stencil were removed. The blank was then soaked in a cleaning neutralizing solution for approximately 30 seconds and cleaned with a cloth. It was then rinsed with water and a different cloth, rinsed with ethanol, and dried. This process was repeated with grids for strain measurement: square grids, measuring 2.54 mm x 2.54 mm; and circle grids, measuring 2.54 mm in diameter.

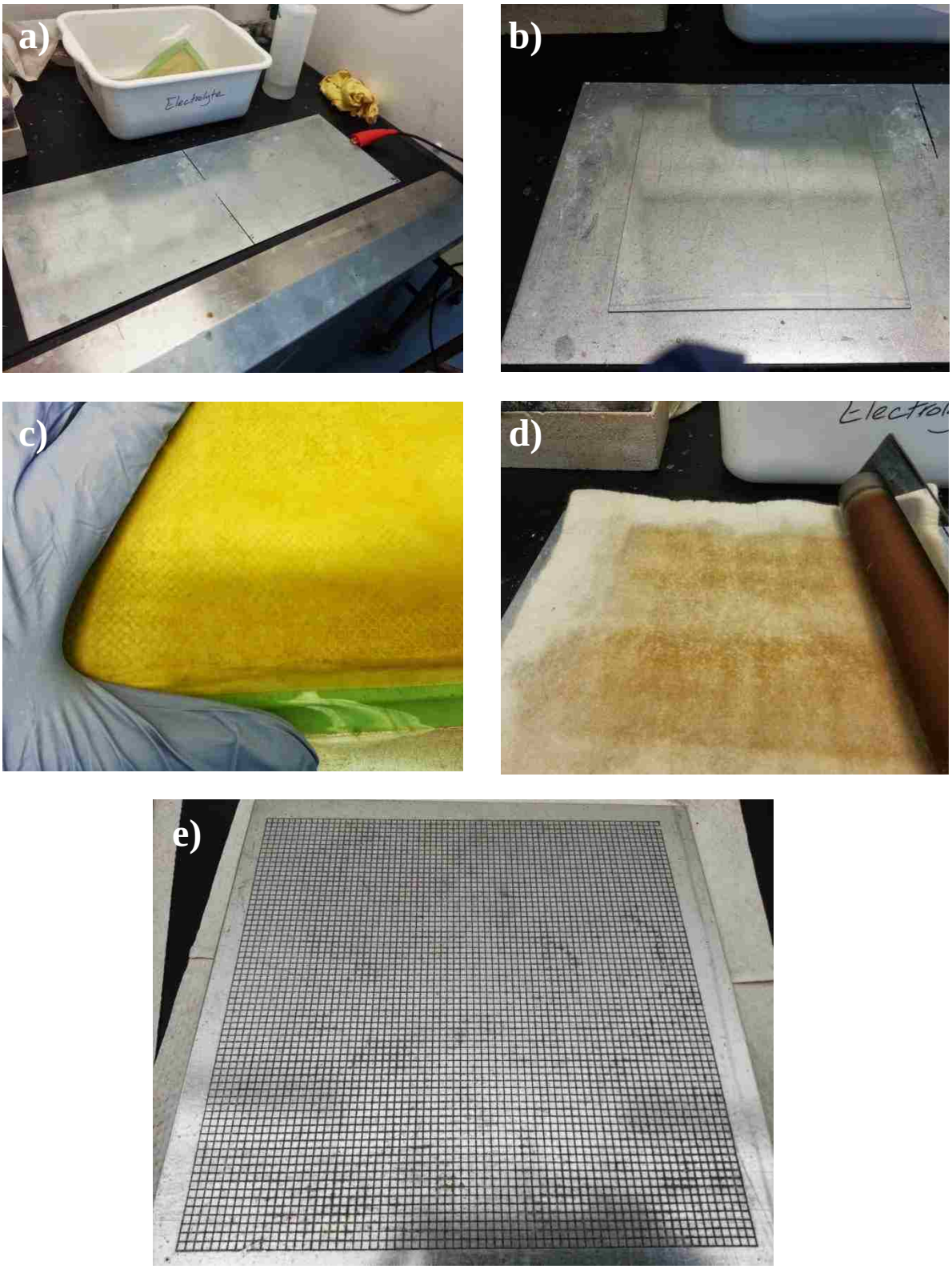

Figure 3.1: Electro-etching procedure: a) the sacrificial blank; b) the blank to be gridded; c) the gridding stencil; d) the metal roller and felt wick; and e) the blank after gridding

3.3 Nakazima Testing

Quasi-static tests were performed on a number of blanks to better understand the evolution of voids in the microstructure of DP600 steel. Figure 3.2 shows a diagram of the Nakazima test.

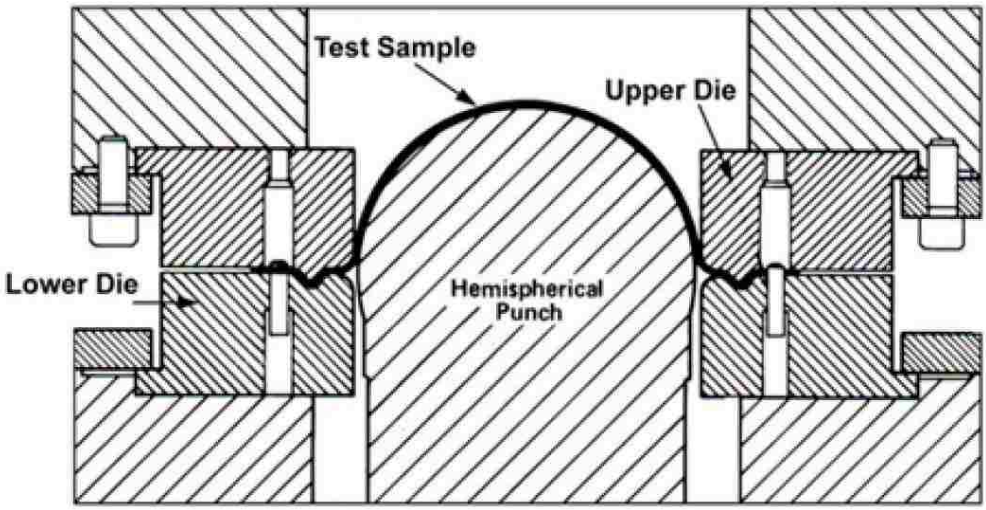

Figure 3.2: Nakazima test [65]

The Nakazima tests at CANMET were conducted using a 101.6 mm diameter hemispherical punch with a 110 mm die aperture, and 289 kN holding force. Blanks were prepared by CANMET with a speckled pattern for digital image correlation (DIC) analysis and some were used from the batch of blanks prepared as described in Section 3.2. The test setup and equipment are shown in Figure 3.3.

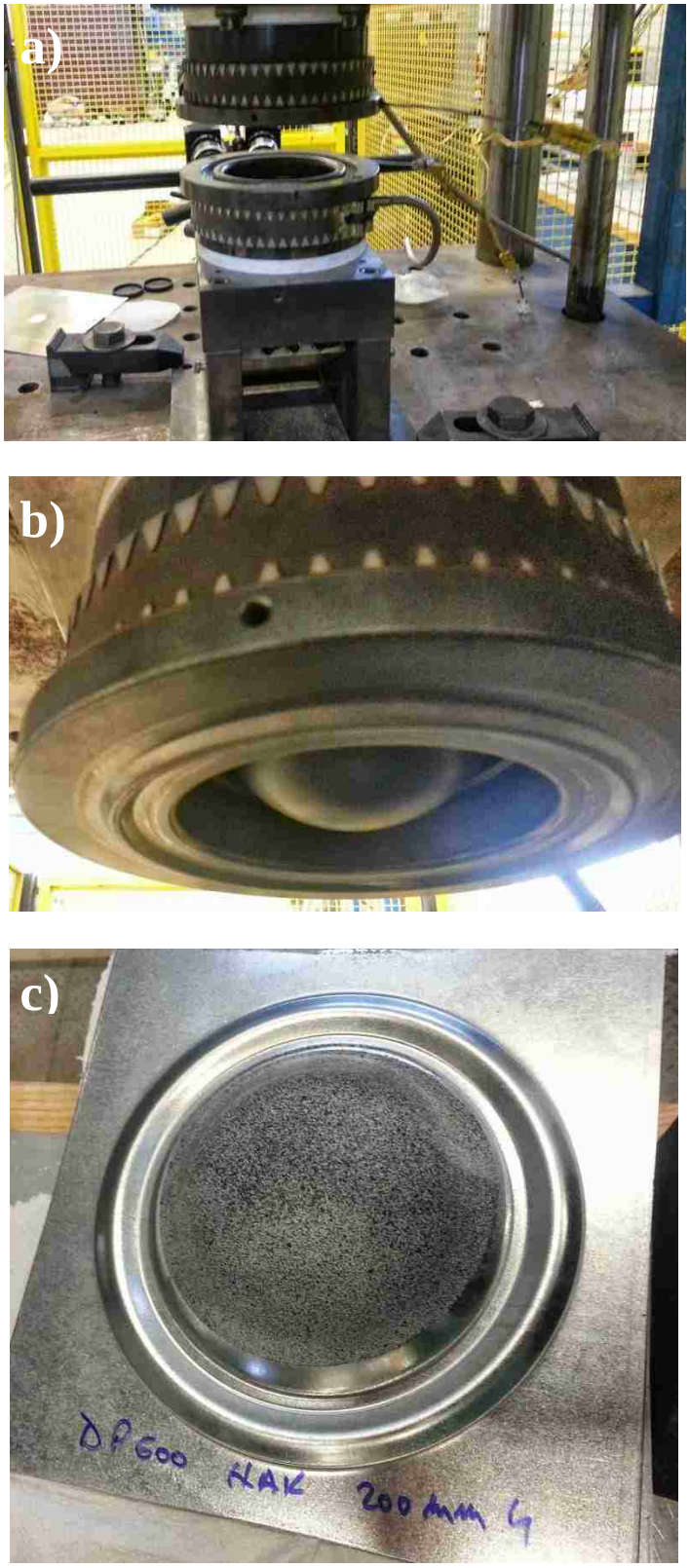

Figure 3.3: a) Nakazima test setup; b) hemispherical punch; c) formed specimen showing the DIC speckled pattern.

3.4 Electrohydraulic Forming Tests

The EHF tests were performed at the Ford facility in Dearborn, Michigan, USA. Gridded sheet metal blanks of DP600 were formed using both EHFF and EHDF methods. In EHFF, a forming ring was used to guide the blank during initial forming. In die forming, EHDF, a complete 34° conical die, Figure 2.10, was used to form the specimen; the sheet metal filled the die when sufficient input energy was provided.

The following procedure was used to conduct the die forming tests. An overview of the process was provided in Section 2.2.4; test setup as shown in Figure 3.4.

1. A coiled copper wire was first set between the electrodes to bridge the connection and steady the pulse
2. The chamber was filled with water
3. A blank was then placed on top, followed by the 34° conical die
4. The vacuum hose was attached to the top of the die
5. The ram was lowered to clamp the piece with the die
6. Vacuum was created between the blank and the die using a vacuum pump to reduce resistance to the sheet's motion
7. Finally, the voltage level was set and the discharge was initiated to form the piece

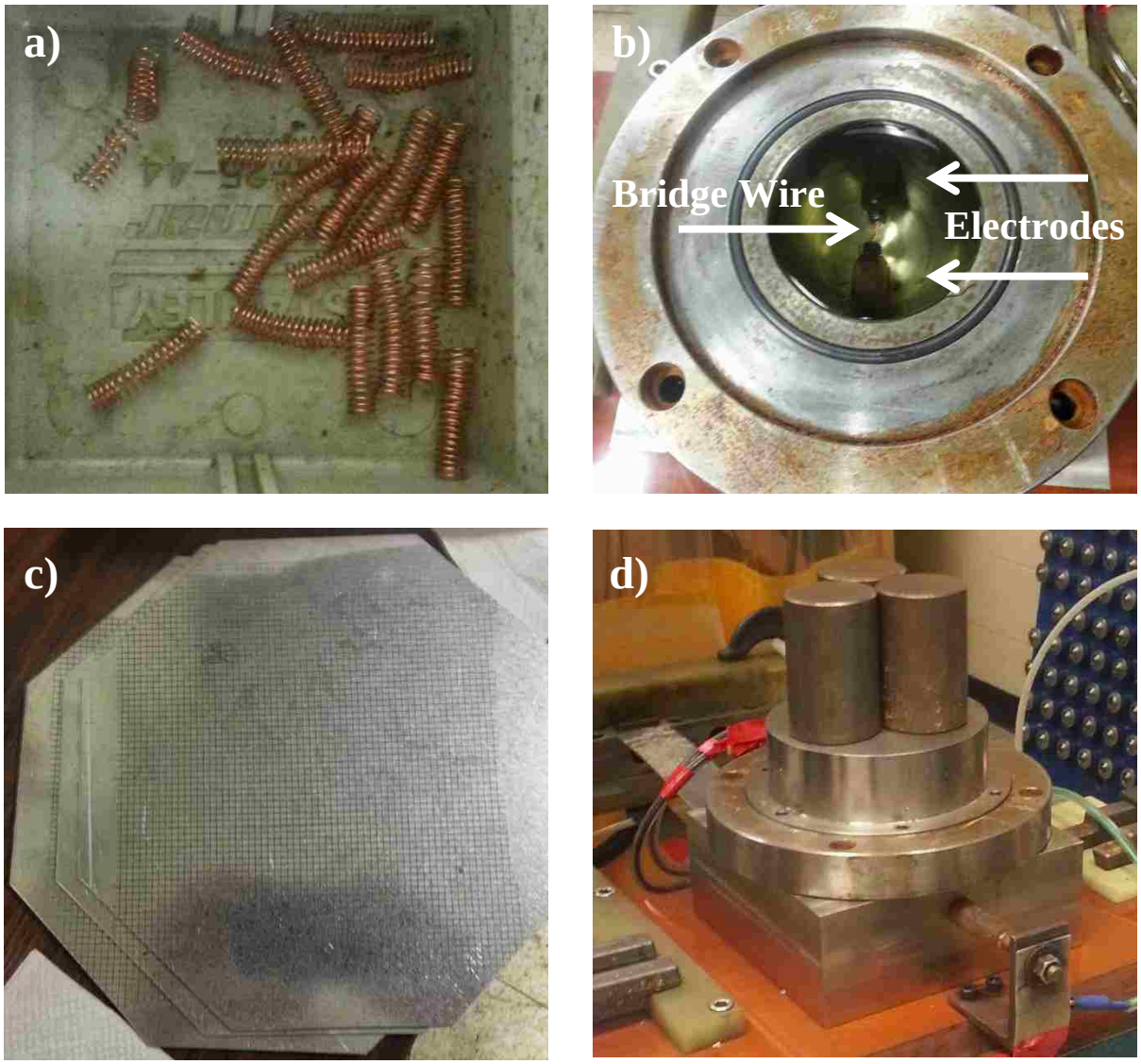

Figure 3.4: EHDF process: a) bridge wire; b) filled water reservoir; c) gridded blank; d) setup before discharge with ram raised.

3.5 Macro-strain Measurements

After specimens were formed, both in quasi-static and EHF conditions, the strain in the sheet was measured using the FMTI grid analysis software and camera. A screenshot of a deformed grid is shown in Figure 3.5. The camera was a Pentax TV lens camera. The software first required the type of grid (circle or square, for example) to be chosen and calibrated. After this step, a few undistorted grids were captured using the camera to verify that the system was calibrated. Grids were measured from the base of the formed specimen in a straight line over the apex to the base on the opposite side, Figure 3.6. This process was then repeated along a direction 90° from the previous measurements to acquire strain measurements parallel to and perpendicular to the rolling direction. After the grids were measured, the strain data were output to a text file and then transcribed into an Excel spreadsheet for further analysis.

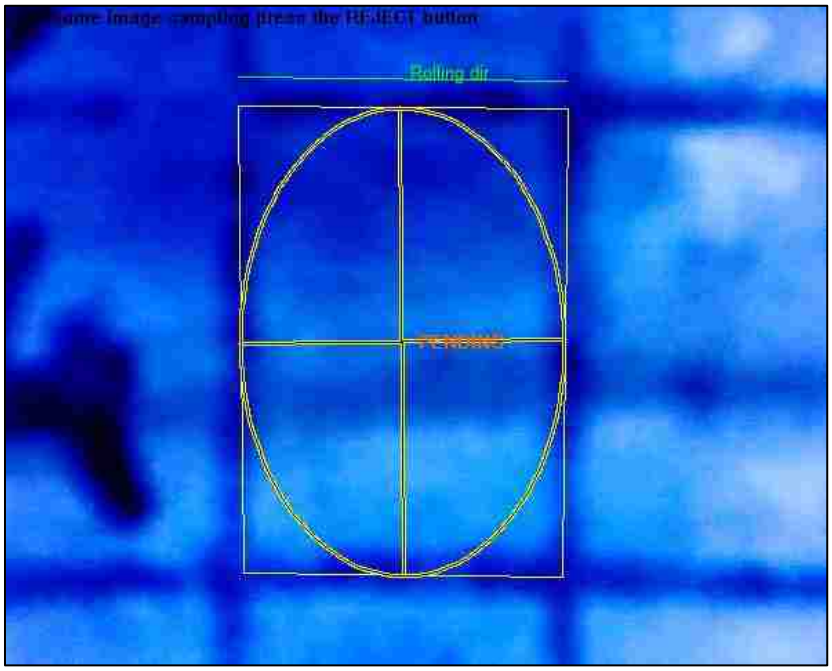

Figure 3.5: Screenshot of FMTI grid analysis software

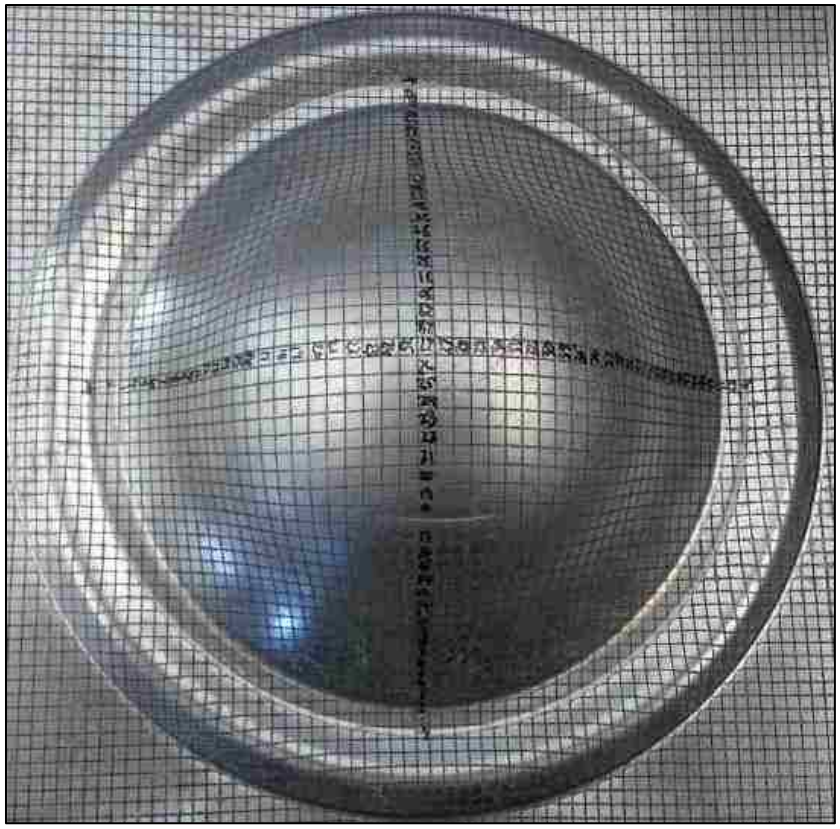

Figure 3.6: Nakazima specimen numbered for strain measurement

An initial set of strain measurements described the strain distribution across the different types of specimens. A second round of strain measurements was taken on either side of the cracks on the specimens. For those samples that did not fail, measurements were taken at a neck or as close to the apex as possible, because the surfaces of some of the EHF specimens were severely damaged at the apex, Figure 3.7, which prevented grid analysis there. These strains were measured to gain an understanding of the level of deformation accommodated by the steel in the different processes.

Figure 3.7: Severe surface damage to the apex of EHDF sample preventing grid analysis

A final set of strain measurements were collected at critical points on the samples from each type of forming operation. The Nakazima specimen measured had a split where strain was measured on either side, as did the EHFF sample. The EHDF sample had formed a neck and strain was taken across the neck. These were measured to obtain an example of the strain level at which the microstructure could no longer accommodate further damage.

3.6 Metallographic Characterization

3.6.1 Metallographic Preparation

The as-received DP600 was characterized using common metallographic techniques. The sheet steel thickness was 1.5 mm. Samples used for observation were cut approximately 5

mm by 20 mm. Formed samples from the Nakazima, EHDF, and EHFF processes were cut using electric discharge machining (EDM) in a pattern shown in Figure 3.8. The plan view samples were 10 mm by 15 mm, the transverse view samples were 15 mm by 5 mm, and the longitudinal view samples were 10 mm by 5 mm.

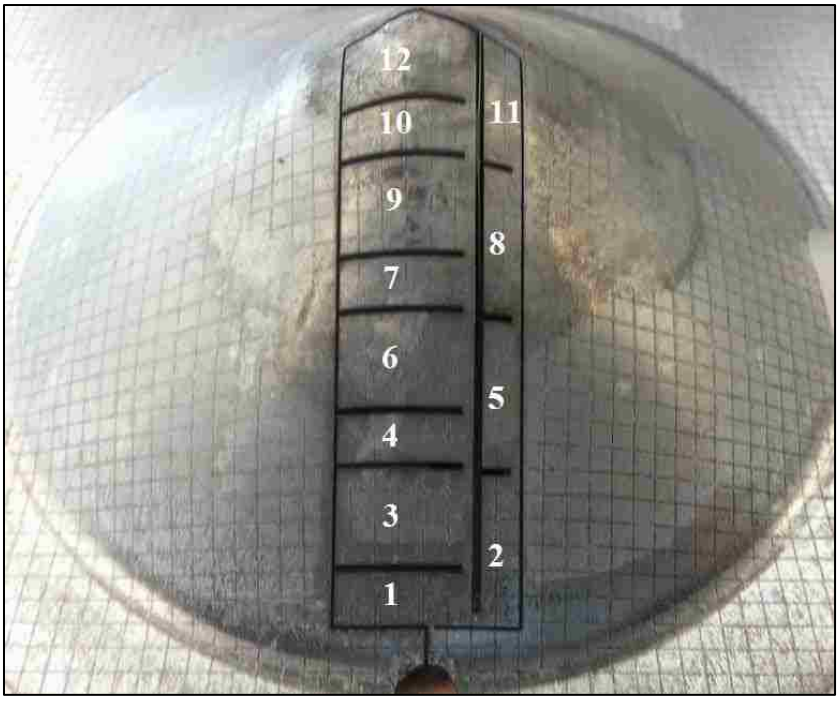

Figure 3.8: EHDF specimen cut using EDM. Samples: 1, 4, 7, 10 - Longitudinal; 2, 5, 8, 11 – Transverse; 3, 6, 9, 12 – Plan.

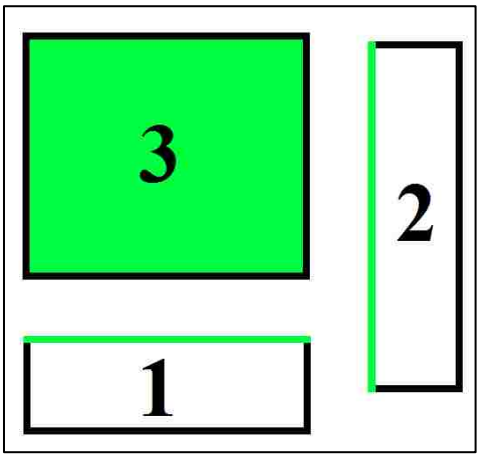

Figure 3.9: Observation surfaces of samples

All metallographic samples were mounted in diallyl phthalate. The 381-mm (1.5 inch) diameter specimens were manually ground using four grits of silicon carbide sandpaper: 240, 320, 400, and 600. Rough polishing consisted of a 9 µm diamond step. 1.0 µm and 0.05 µm alumina suspensions were used for fine polishing. The polished samples were pre-etched using a 2% Nital solution to remove any disturbed metal at the surface. The solution was absorbed into a cotton ball and lightly applied to the surface of the sample. This pre-etch was removed by a short polish with 0.05 µm alumina suspension. Final etching with 2% Nital was applied to the surface for approximately 8-10 seconds before rinsing with water to stop the reaction.

3.6.2 Image Analysis

EHFF and conical EHDF samples, as well as domed Nakazima specimens were sectioned up the side to the apex using wire EDM, as shown previously in Figure 3.8. The sections were designed so that the plan view, longitudinal view, and transverse view could all be observed for metallography. Optical microscopy was performed at 50x, 100x, 200x, 500x, and 1000x magnification using a PAXcam system. The images were then adjusted for contrast using Photoshop Elements and analyzed with Clemex Vision Pro software to determine the volume fraction of martensite and voids in the microstructure, as well as the grain size of ferrite and martensite.

3.6.3 Void Volume Fraction

The void volume fraction was measured using Clemex Vision Pro software following ASTM E1245-03(2008) [64]. In the case of void volume fraction, samples had not yet

been etched. Before micrographs were taken with the PAXcam system, the surface of each sample was quickly wiped with 2% Nital etchant (less than one second) to only remove the disturbed surface layer with high energy to reveal any voids that might be covered by brushed metal due to grinding. The contrast-adjusted micrograph was opened in Clemex and the Gray Threshold tool was used to assign the colour red to the range of gray representing the voids in the microstructure. The remaining matrix was coloured yellow to retain a visual contrast. This adjustment is shown in Figure 3.10. The area percent was found under the Field Measure tools and was inserted into the results window and recorded in a spreadsheet. This process was repeated for ten micrographs from each transverse view sample, denoted as samples 2, 5, 8, and 11 in Figure 3.8.

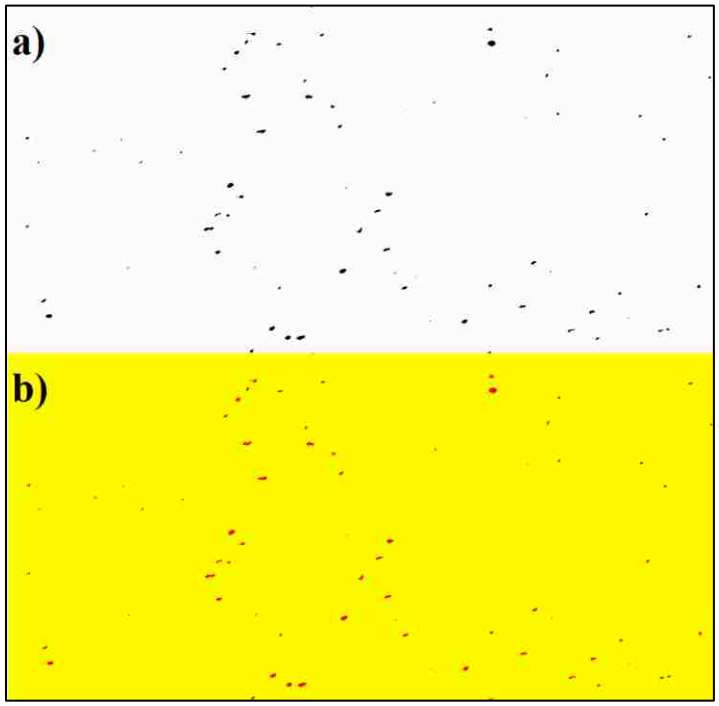

Figure 3.10: Void volume characterization using Clemex Vision Pro

The transverse samples used for void volume fraction quantification were not taken directly from the line of previously measured strains. To compensate for this discrepancy,

the strains in these samples were estimated based on the assumption that strains at a certain height on the dome or cone are equal around the specimen. The strain pattern in Figure 3.11 supports this assumption as it can be observed that the strain levels in the specimens appear to be changing with height as approximately concentric circles.

Void volume fraction was also calculated at the fractured or necked points on the samples mentioned in Section 3.5 to observe the level of accumulation of voids at necking and fracture. The same process was used; however, the viewing plane of the sample was determined by the orientation of the neck or crack, unlike the previous steps where the transverse orientation was chosen.

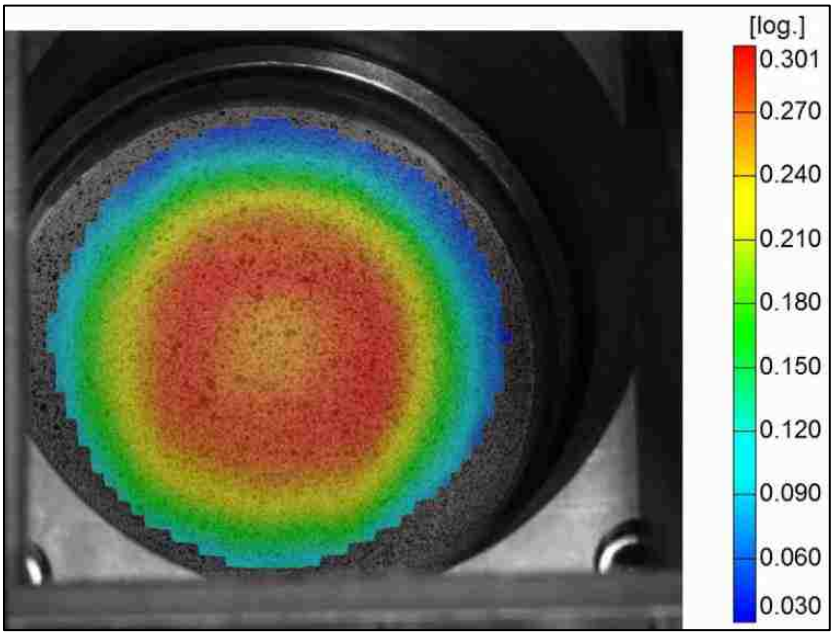

Figure 3.11: Nakazima specimen strain map

3.6.4 Grain Size

Ferrite grain size was measured according to two techniques specified in ASTM E112-13 [65]. One technique was the manual statistical method, performed in Clemex using the

Measure Line tool, shown in Figure 3.12. Three micrographs taken at 500x or 1000x magnification were used from each longitudinal view sample, noted as samples 1, 4, 7, and 10 in Figure 3.8. Out of the total number of measurements on each micrograph, approximately half were made on the major (horizontal) axis of the grains and the other half were through thickness. The relative accuracy was also calculated according to the ASTM standard to ensure acceptable results. First the 95% confidence interval was calculated using Equation 3.1, and then it was used as input for the relative accuracy (*%RA*) in Equation 3.2, each shown below:

$$\mathbf{95\%}\ \boldsymbol{CI} = \frac{\pm \boldsymbol{t} \cdot \boldsymbol{s}}{\sqrt{\boldsymbol{N}}} \tag{3.1}$$

where *t* is a confidence internal multiplier chosen from a table based on the number of fields counted, *s* is the standard deviation of the values, and *N* is the number of measurements.

$$\%\boldsymbol{RA} = \frac{\mathbf{95\%}\ \boldsymbol{CI}}{\bar{\boldsymbol{x}}} \tag{3.2}$$

where $\bar{x}$ is the mean grain size; a relative accuracy of 10% or lower is considered acceptable precision [65].

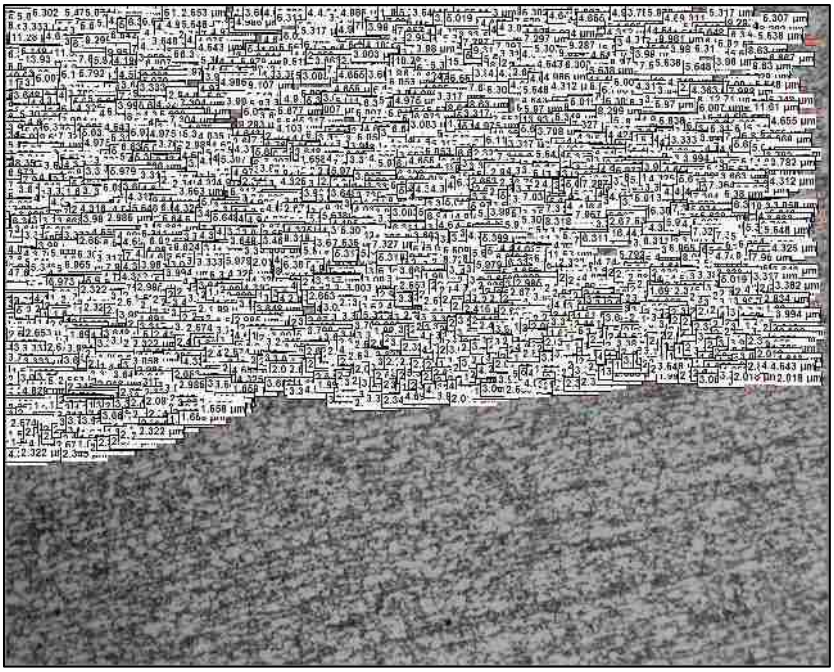

Figure 3.12: Manual grain size measurements using Clemex

The other technique to measure grain size was the planimetric, or Jeffries' method. In this method, each grain within a 5000 mm^2 circular template was counted, the total was multiplied by a Jeffries' Multiplier, *f*, and the mean size was interpolated from a table in the ASTM E112-13 standard [65]. Three micrographs were used for the average grain size calculation from each sample. The result of this process is shown in Figure 3.13, where each grain is represented by a dot on the micrograph.

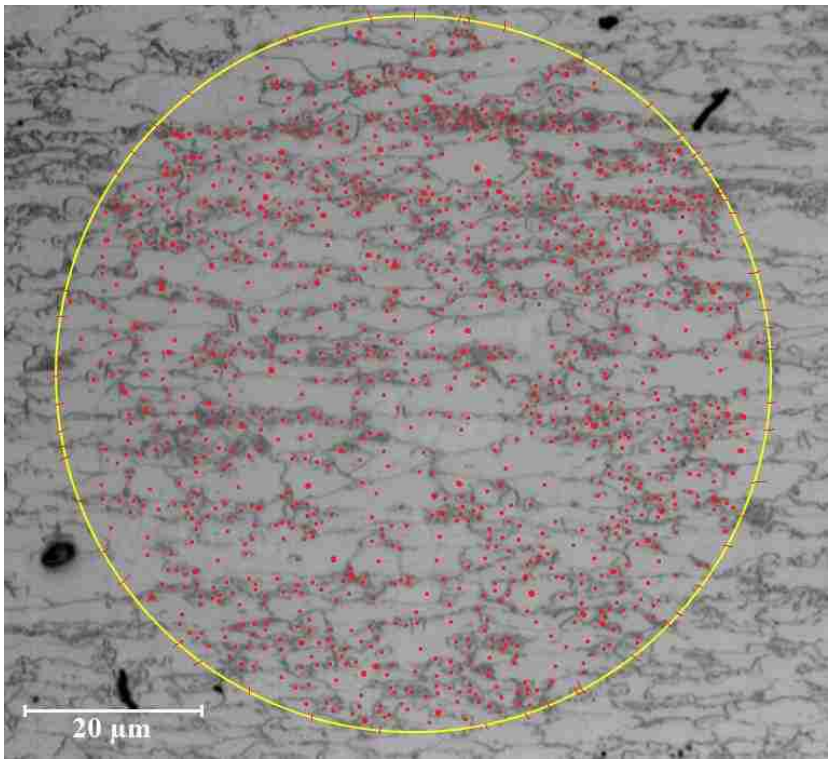

Figure 3.13: ASTM E112 Planimetric procedure result

3.6.5 Martensite Volume Fraction

Martensite volume fraction was measured using Clemex Vision Pro according to ASTM E1245-03 (2008) [64]. The microstructure was first adjusted for contrast using Photoshop Elements to exaggerate the difference in grayscale between the martensite and ferrite. The micrograph was then analyzed for area percent, similar to the process used in Section 3.6.3 for the void volume fraction analysis. The grayscale range representing martensite was coloured red and quantified as an area percent, as shown in Figure 3.14. The ferrite matrix was coloured yellow for visual contrast afterwards.

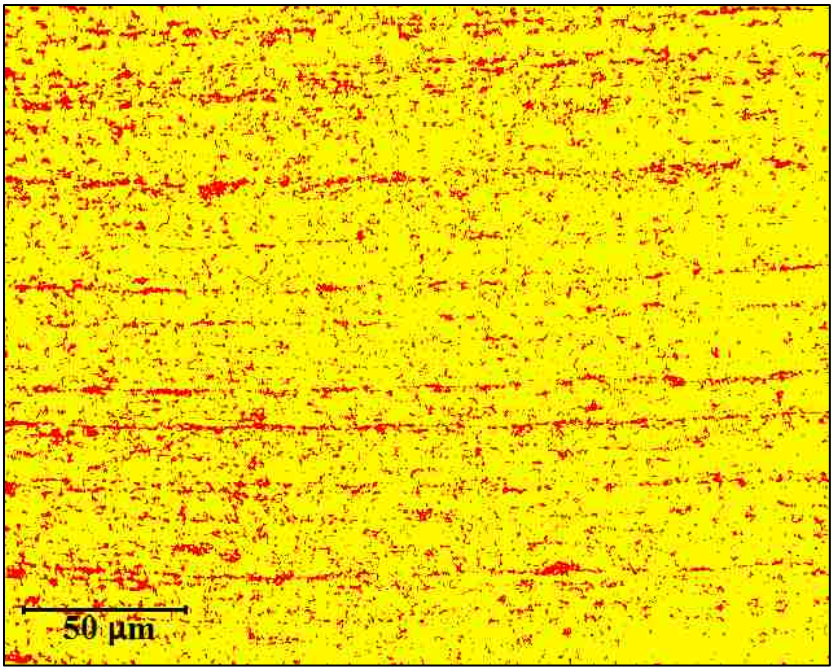

Figure 3.14: Martensite volume fraction micrograph after Clemex grayscale quantification

3.6.6 Fractography

To determine the primary mechanism leading to fracture and the type of fracture resulting from testing, one side of a crack was cut from a Nakazima specimen and from an EHFF specimen for SEM observation and additional void volume fraction quantification were conducted. The observation was not carried out on EHDF specimens as none of the DP600 EHDF specimens experienced failure in testing up to 15 kV. The crack face in each case was clamped standing up on the SEM stage, and the entire surface was observed. The other half of each crack face was mounted for void quantification.

Chapter 4 :

Experimental Results

4.1 Strain Measurements

Strain measurements were taken using the FMTI system described in Chapter 3. Figure 4.1 shows the peak strains measured in quasi-static (QS) conditions, in this case Nakazima testing, electrohydraulic free forming (EHFF), and electrohydraulic conical die forming (EHDF). They run in a band up to 0.5 strain just above the 45 degree line of equi-biaxial strain.

Figure 4.2 shows the mean peak strains for the Nakazima samples tested at the CANMET laboratory. Three patterns were tested: DIC speckle pattern, listed as DIC; half DIC and half square grid markings, listed as DIC/GRID; and entirely square grid pattern, listed as GRID. The values are contained in an area bounded by major and minor strains from 0.2 to 0.4.

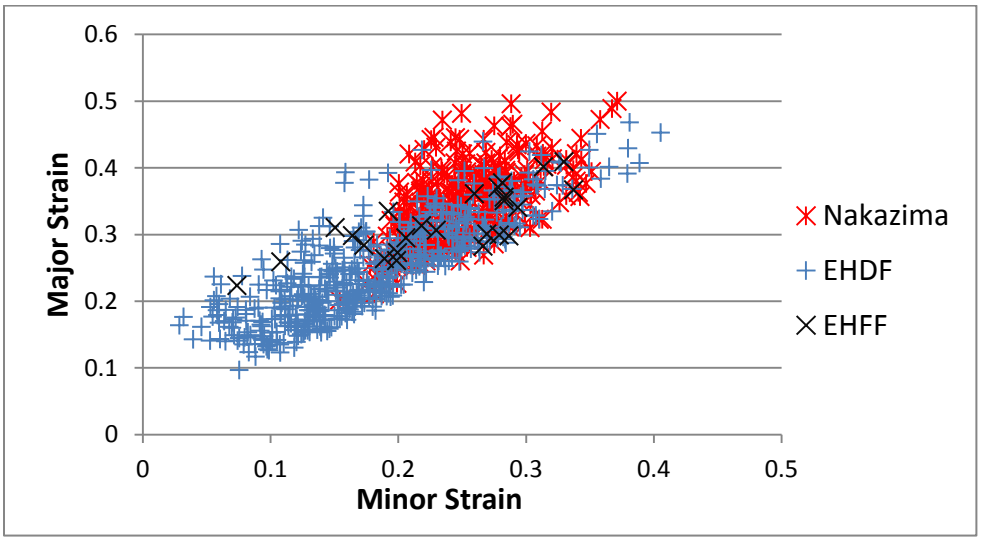

Figure 4.1: FMTI macro-strain data

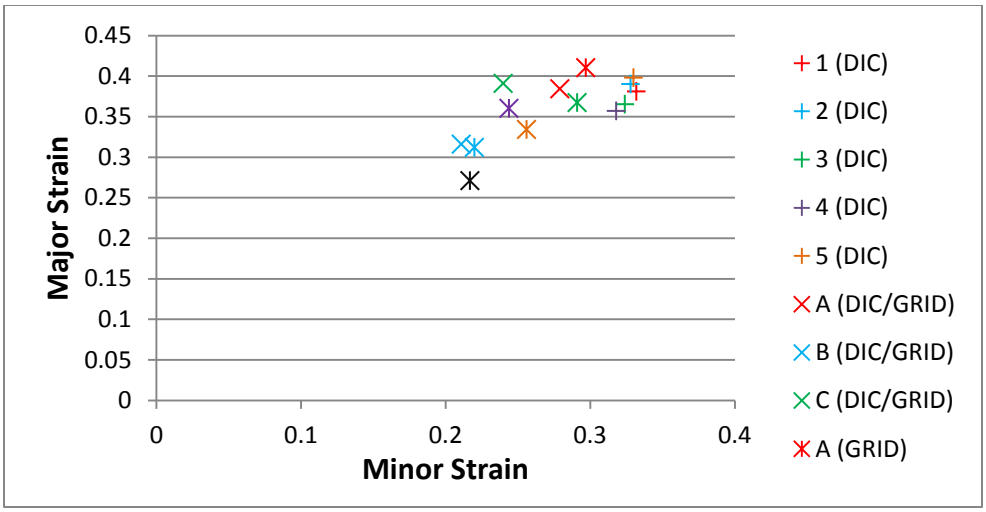

Figure 4.2: Nakazima mean peak strains

Figure 4.3 shows the strain map obtained from the Nakazima test performed at CANMET in Hamilton, Ontario. The strains were measured using the DIC method, captured using two cameras for depth perception. The progression was shown from the start of the process to fracture in video format; a frame from the video of specimen '1' being formed is shown at fracture in Figure 4.3. A maximum strain is noted along the crack in the upper half of the specimen.

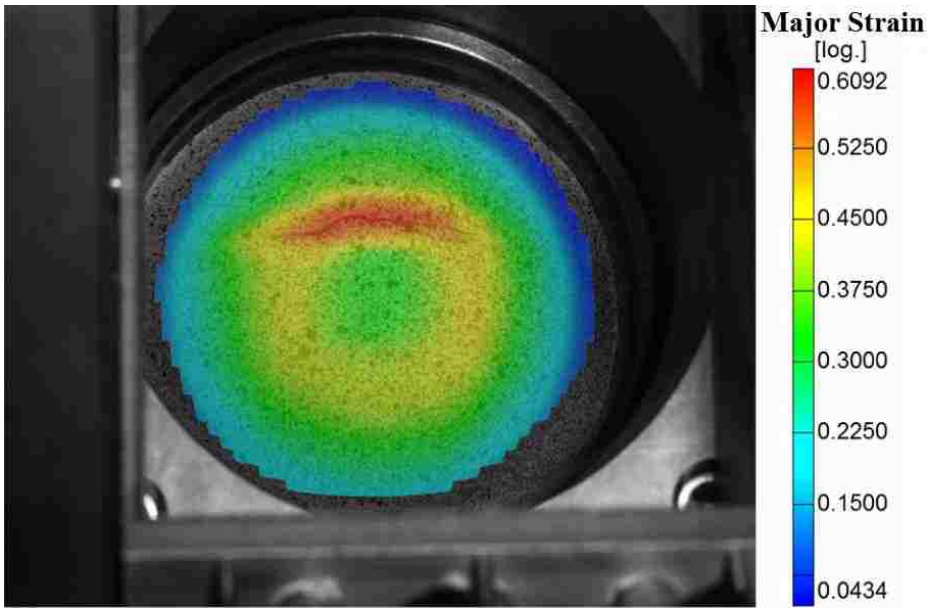

Figure 4.3: DIC strain map of deformed Nakazima specimen at failure

Figure 4.4 and Figure 4.5 show the strain distribution across the specimen as a result of forming in the Nakazima and EHDF conditions, respectively. RD is the rolling direction in the figure. The distance shown on the x-axis refers to the number assigned to each grid square on the specimen for FMTI strain analysis, as seen in Figure 3.6 and Figure 3.7. It was noted that the QS test result exhibits peaks on both sides of the specimen centre. The EHDF specimen exhibited a single peak at the sample centre.

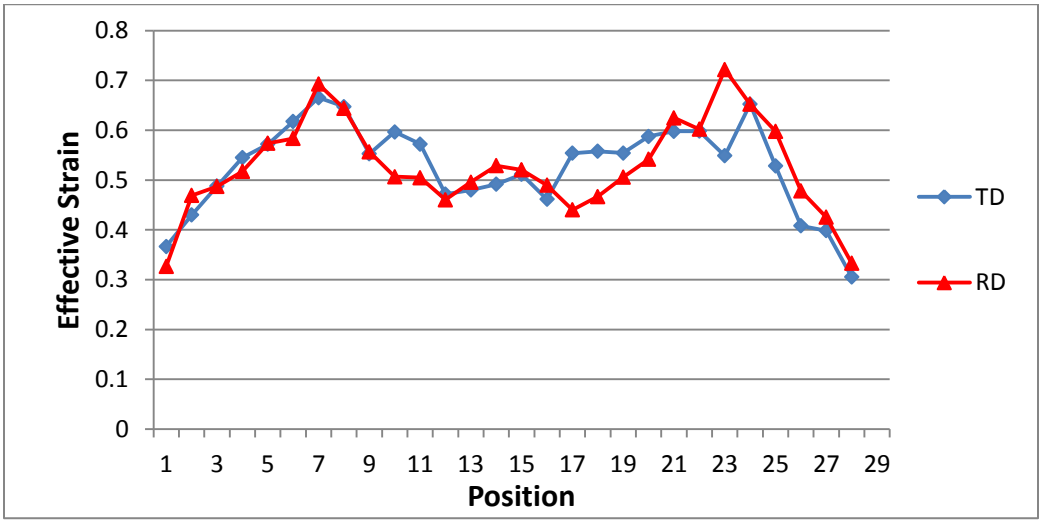

Figure 4.4: Strain distribution across a Nakazima specimen

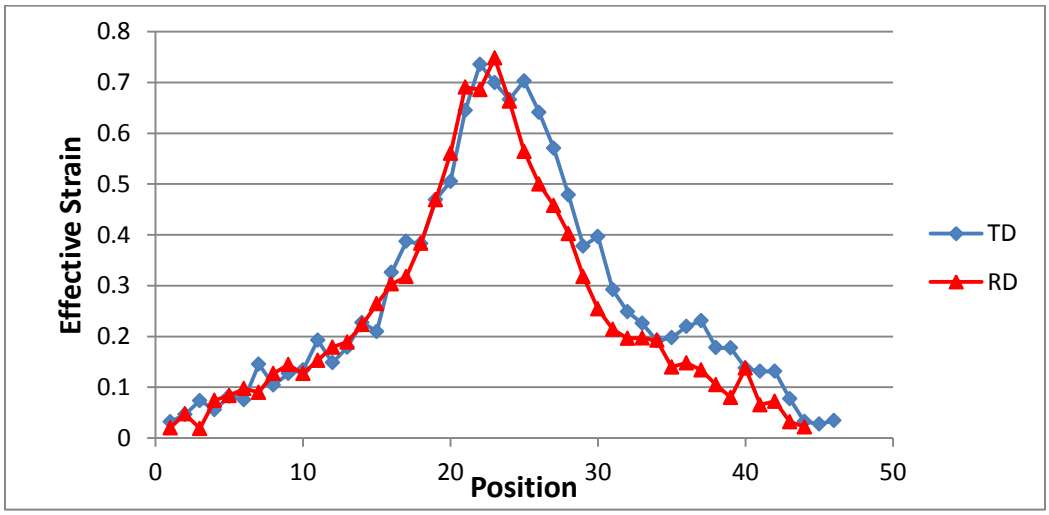

Figure 4.5: Strain distribution across an EHDF specimen

Figure 4.6 shows the location of safe combinations of strain on EHDF specimens compared to the forming limit curve for quasi-static conditions, shown in black.

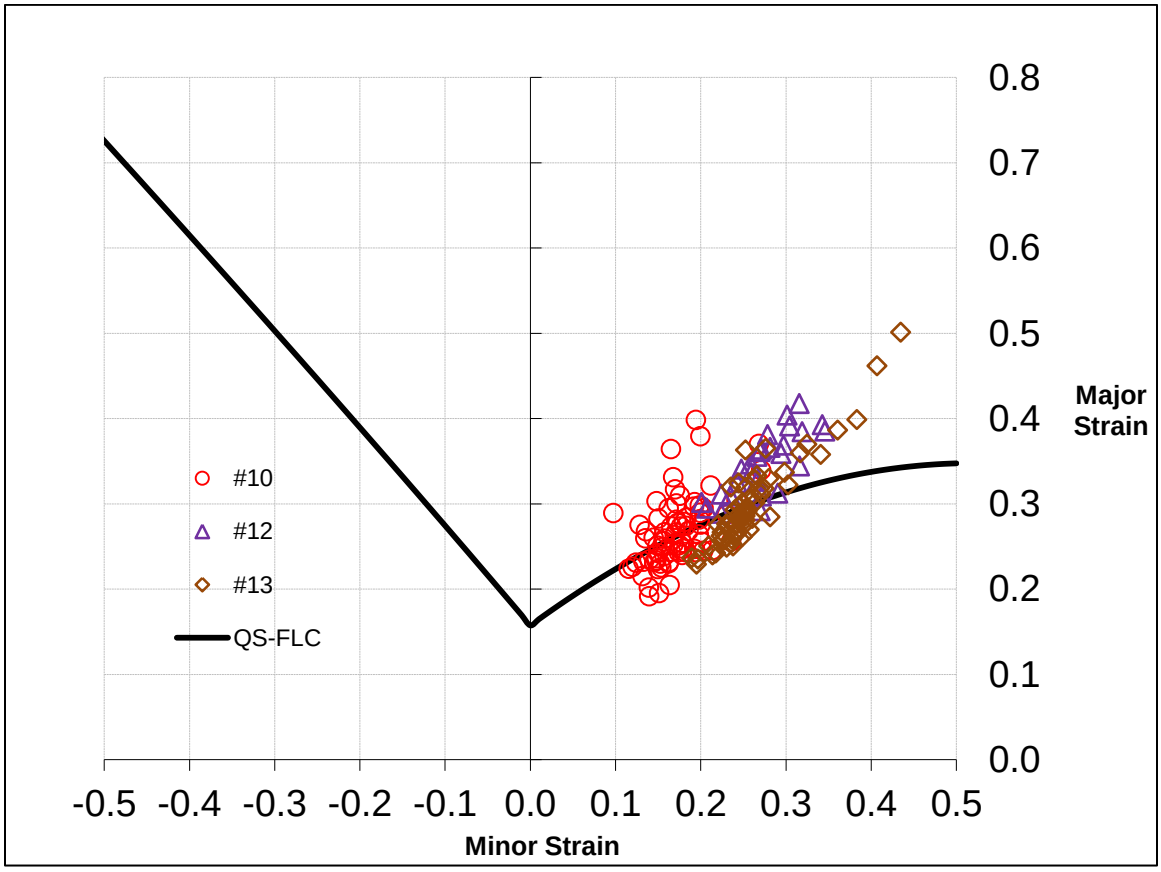

Figure 4.6: Forming limit curve for DP600 EHDF tests, true strain. The numbers indicate the test specimen from which the strain data was measured and the QS forming limit curve is shown.

4.2 Void Volume Fraction

The level of damage in the microstructure was quantified by the void volume fraction in the microstructure. As described in Section 3.6.3, Clemex Vision Pro was used to quantify the amount of grayscale representing voids in the microstructure as an area percent. The results are presented in Figures 4.7-9.

Figure 4.7 shows the void volume fraction for the Nakazima specimen and how that trend is affected by effective strain applied to the microstructure. Effective strain is the von Mises equivalent strain and is a scalar quantity used to describe the state of strain. Additionally, a final point represented by a hollow marker represents the fracture strain on a sample taken at the split. The plotted points were fitted with an exponential trendline.

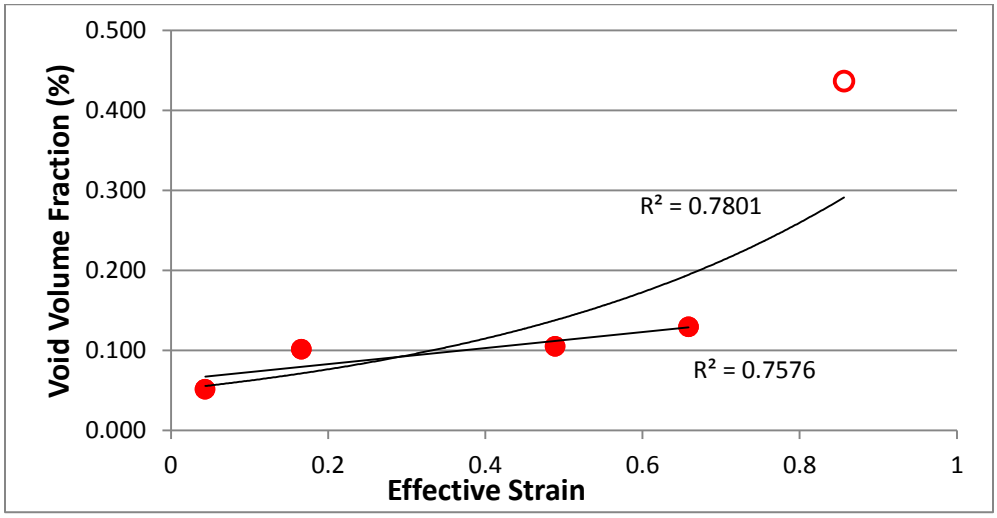

Figure 4.7: Void volume fraction (Nakazima)

Figure 4.8 and Figure 4.9 show the void volume fraction vs effective strains for the free formed and die formed specimens, respectively. Similarly to the plot in Figure 4.7 above, an extreme point of strain is plotted as a hollow marker to show strain and void volume fraction at failure (EHFF) and in a necked area (EHDF) to represent the highest amount of damage that occurred in the microstructure.

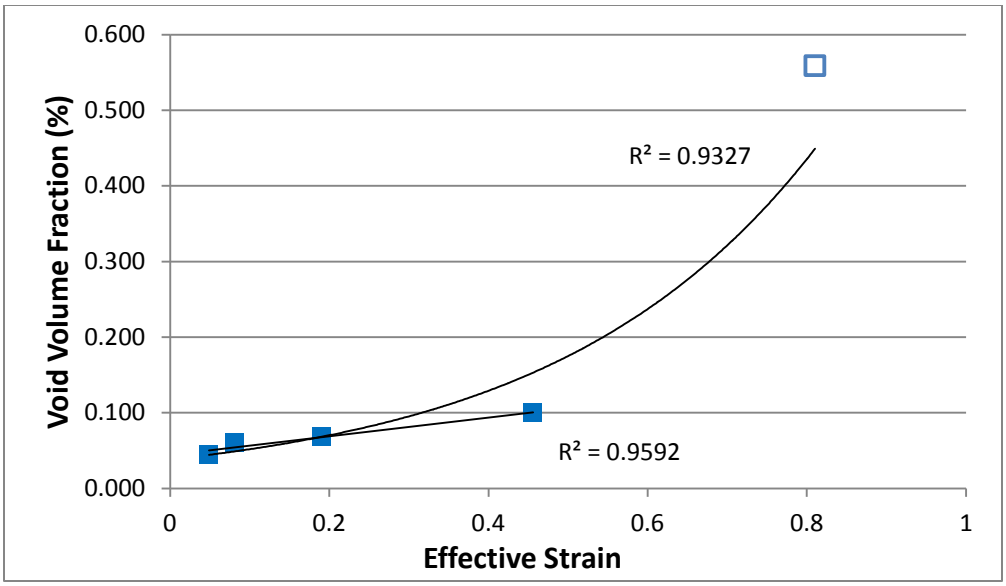

Figure 4.8: Void volume fraction (EHFF)

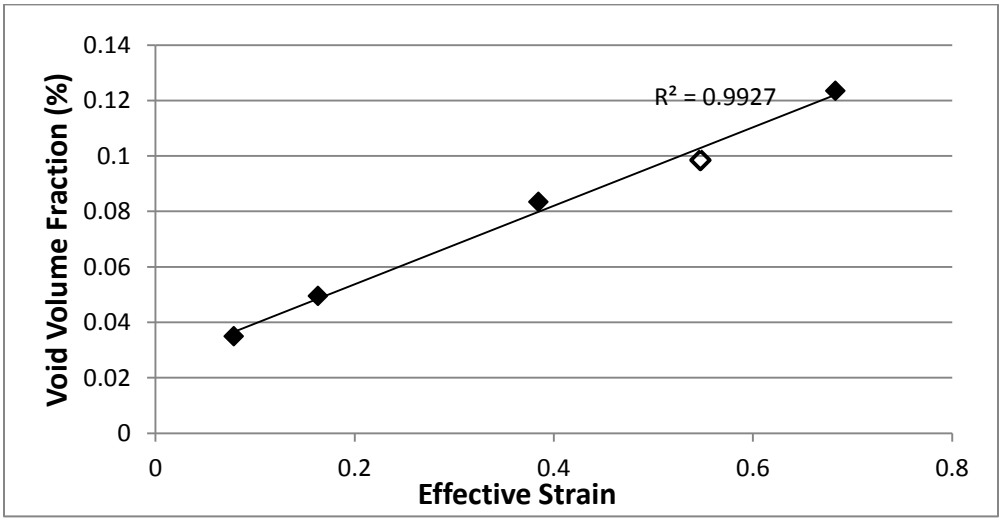

Figure 4.9: Void volume fraction (EHDF)

Figure 4.10 shows the void volume fraction versus effective strain for all three forming operations to show the difference in void evolution with each forming process. It was noted that the EHDF process curve sits below the other two process curves; it indicates that damage accumulation via void formation was lowest for EHDF.

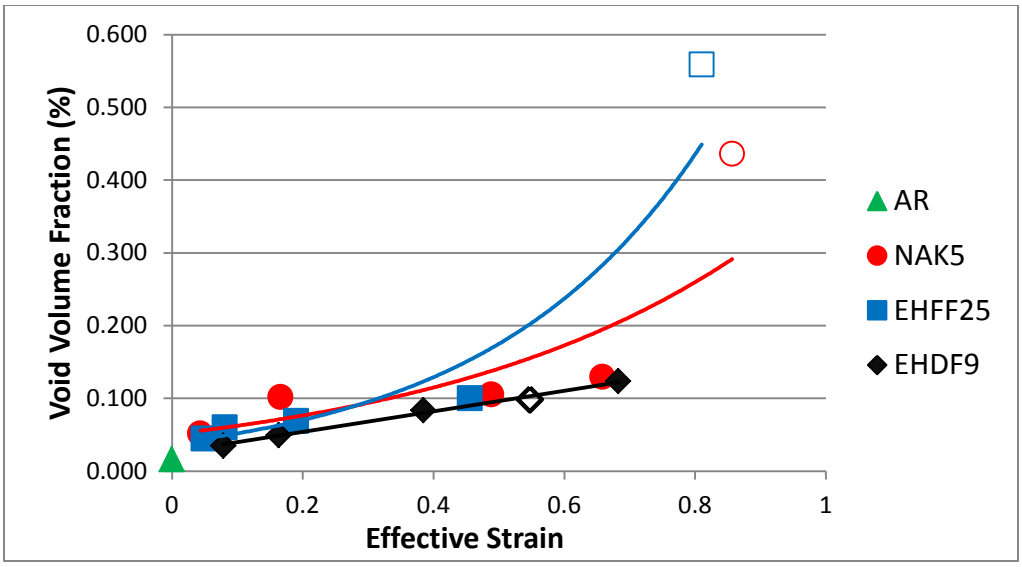

Figure 4.10: Void volume fraction in each type of forming

Table 4.1 and Figure 4.11 show the estimated values and plot comparison of the void volume fraction evolution with increasing strain rate between the two EHF processes. The data shows that the void fraction increases with strain rate. Strain rates for these processes are noted to increase toward the centre of the formed sheet.

	EHDF				**EHFF**			
Distance from edge (mm)	8	23	38	53	7	22	37	52
Strain rate (s^{-1})	2610	4270	6080	15340	940	1910	3070	3820

Table 4.1: Strain rate estimates for EHDF and EHFF [68]

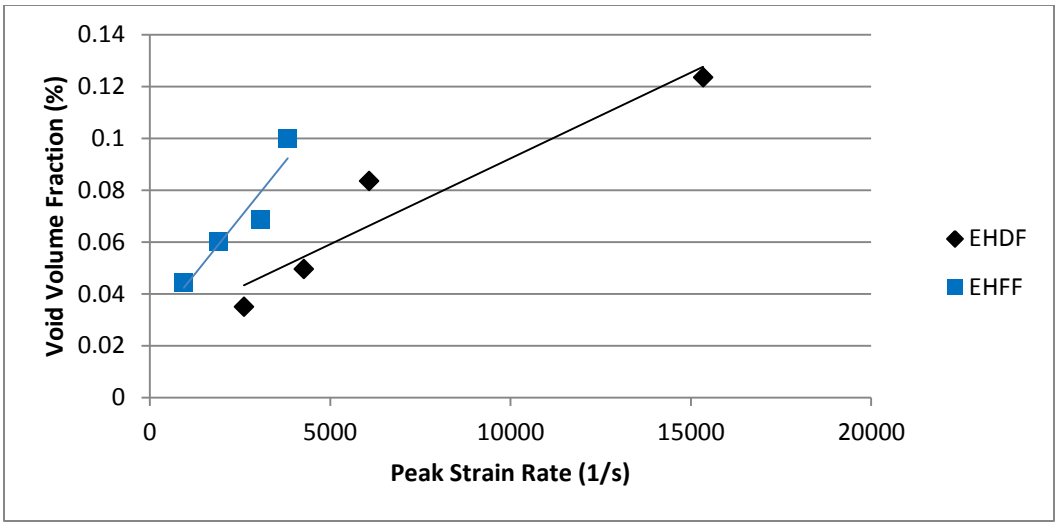

Figure 4.11: Void volume fraction vs strain rate for the EHFF and EHDF processes

4.3 Grain Size

The average ferrite grain size was measured using two methods, as described in Section 3.6.4, according to ASTM standards E112-13. The results of these measurements are shown in Figure 4.12 and Figure 4.13, and are grouped by the section number according to Figure 3.8. Figure 4.12 displays the results of the grain size measurements using Clemex Vision Pro software as shown in Figure 3.11.

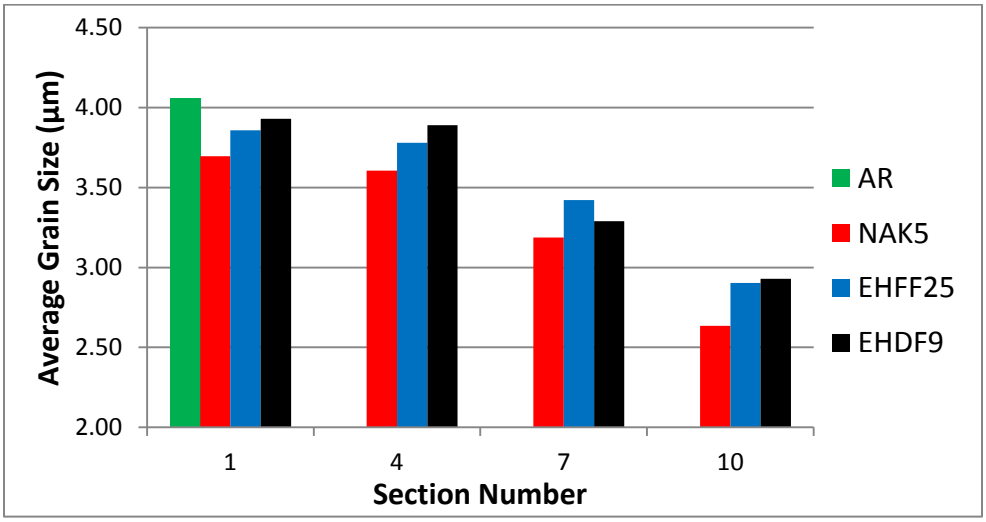

Figure 4.12: Change in grain size with deformation (Clemex)

Figure 4.13 shows the results of the planimetric method of grain size estimation according to ASTM E112-13 and shown in Figure 3.12. A comparison of the average grain sizes calculated by the two methods, Figure 4.14, shows that the methods produce equivalent results.

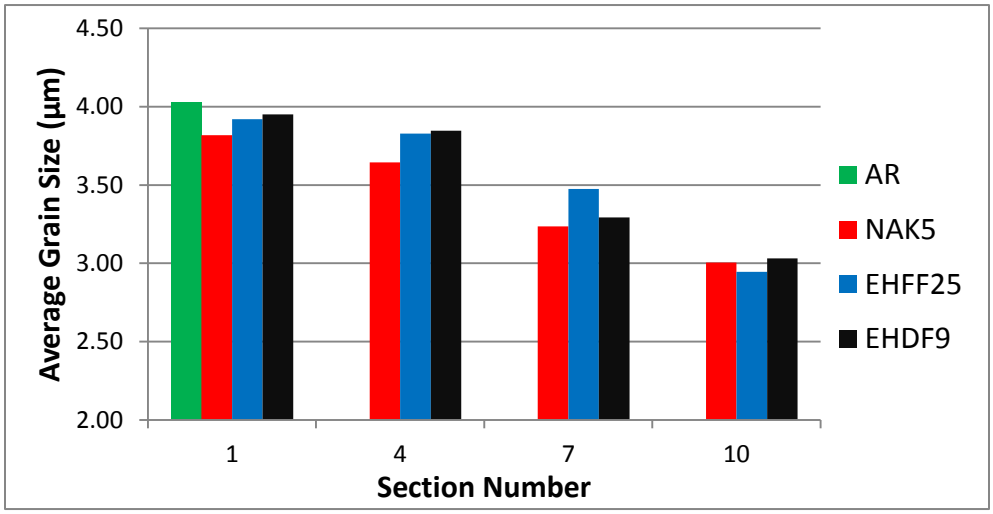

Figure 4.13: Change in grain size with deformation (Planimetric)

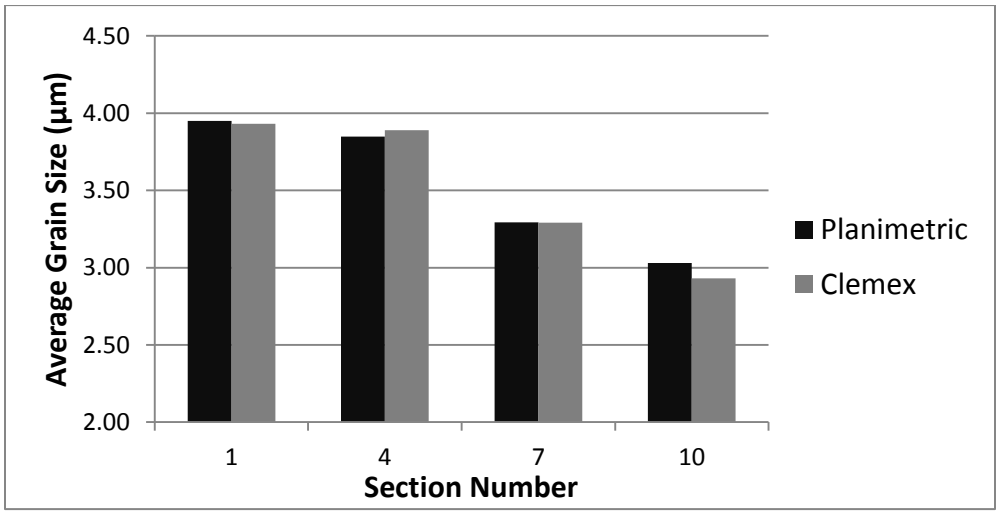

Figure 4.14: Comparison between average grain sizes calculated with both methods in EHDF9

To observe the trend of how grain size varied with the effective strain values, the data was plotted as shown in Figure 4.15. With increasing strain, the average grain size is noted to decrease for all processes.

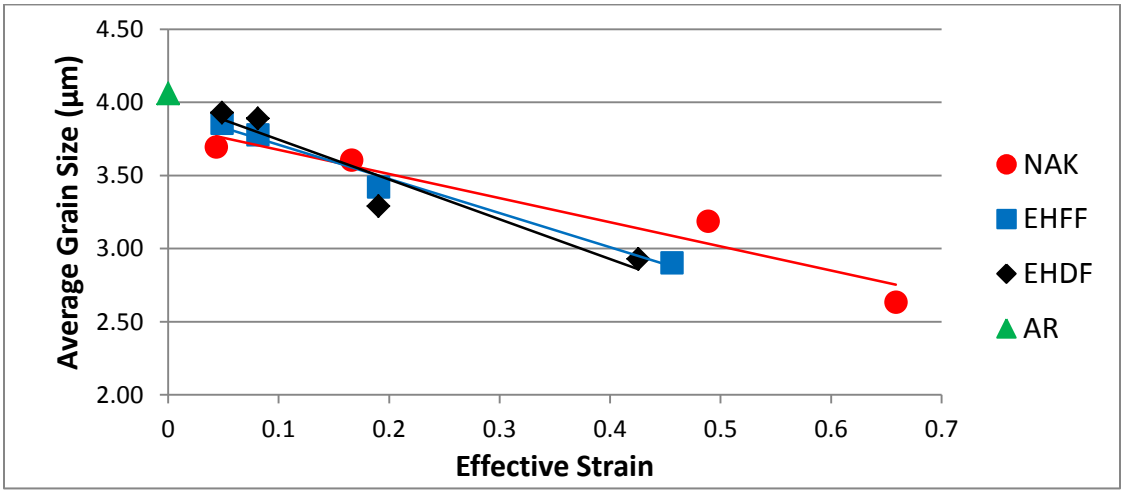

Figure 4.15: Average grain size (Clemex) vs Effective strain

4.4 Martensite Volume Fraction

The martensite volume fraction was obtained according to ASTM E1245 using Clemex Vision Pro as described in Section 3.6.5. Ten micrographs were processed and analyzed, the results of which are shown in Table 4.2.

Material	Mean V_m (%)	Standard Deviation	95% CI	%RA
DP600-AR-L	14.34	2.276	2.825	0.1970

Table 4.2: Martensite volume fraction quantified using Clemex Vision Pro

4.5 Fractography

SEM was used to document the fracture surfaces of the Nakazima and EHFF specimens and fractographs are shown in Figure 4.16 and Figure 4.17**,** respectively. The fracture surfaces exhibited significant dimpling, which is indicative of ductile fracture.

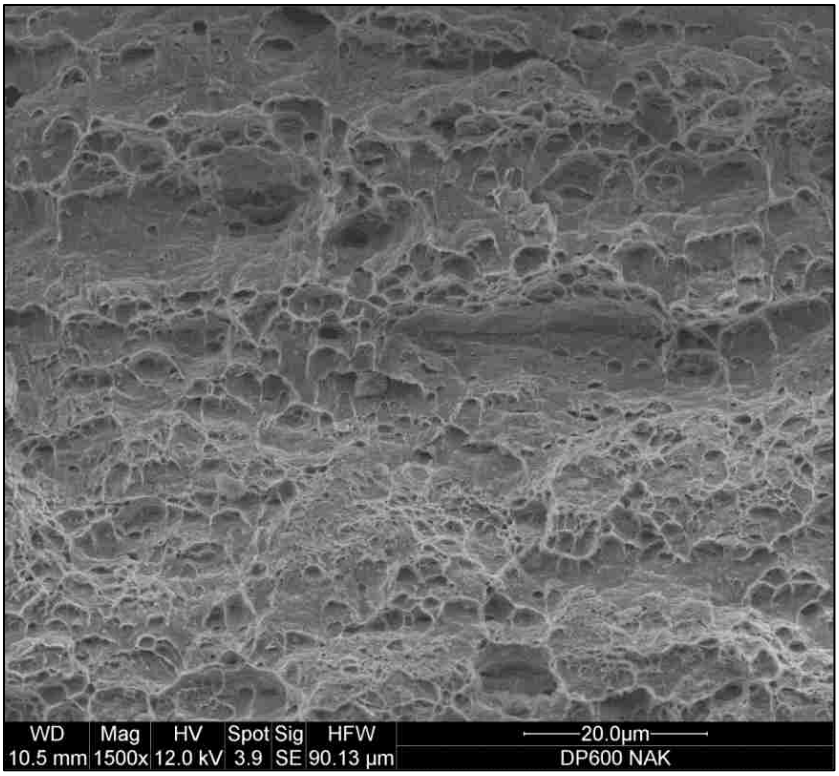

Figure 4.16: Nakazima fracture surface

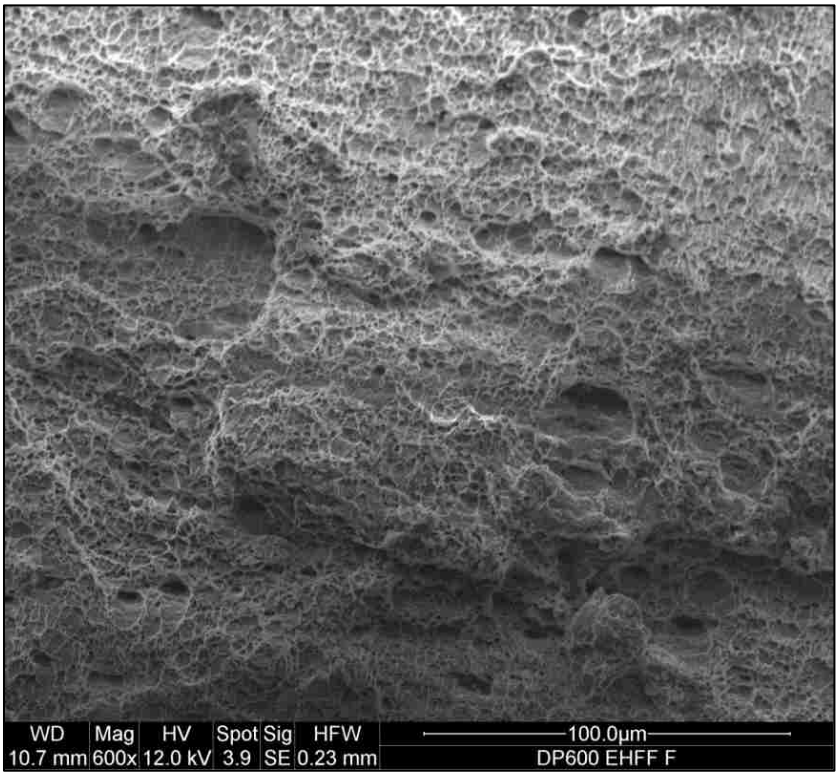

Figure 4.17: EHFF fracture surface

Chapter 5 :

Discussion of Results

5.1 Strain Measurements

For all types of forming (QS, EHFF, EHDF), macroscopic strain measurements were carried out using the FMTI analysis system. Peak strains in the QS (Nakazima), EHFF and EHDF processes were shown in Figure 4.1. These were safe strains, and the measurements were taken in a square grid area at the apex of the specimens. As can be observed in the plot, the Nakazima, EHFF, and EHDF strains were in the biaxial range, which justifies the comparison of the three processes. The other obvious trend in the plot was that the Nakazima strains were, for the majority, greater than those in the EHFF and EHDF specimens. This was attributed to the fact that the Nakazima specimens were tested to failure, but EHDF specimens did not experience failure in testing. Finally, it should be noted that, although the Nakazima specimens were all tested to failure, the extent to which the crack was allowed to progress was not consistent across all specimens: some were stopped according to load drop on the data acquisition screen, while others were stopped by visual observation of failure on a live video feed. As such, increasing strain was allowed to occur after fracture.

To verify that the DIC strain measurements and FMTI strain measurements correlated reasonably well, the average strains around the failure in the Nakazima specimens were plotted in Figure 4.2. It was found that the strain values all fell in the biaxial range and

this validated the FMTI strain measurements taken from the square and circle grid samples.

Figures 4.3 and 4.4 show that the location of failure for the Nakazima specimens occurred offset from the apex of the dome. It was also observed that the failure occurred parallel to the rolling direction of the sheet material.

Figures 4.4 and 4.5 show the contrast of strain distributions observed in the Nakazima and EHDF specimens, respectively. As mentioned previously, the Nakazima specimens failed offset from the apex, where peak strains were also observed. EHDF samples did not fail in the 13 tests at Ford, but the peak strains observed were all at the apexes of the specimens.

Figure 4.6 showed a forming limit diagram for DP600 steel, where the black line represented the quasi-static forming limit curve. It was observed that strains in EHDF trials safely exceeded the quasi-static forming limit curve, thus showing improved formability.

5.2 Void Volume Fraction

Clemex Vision Pro was used to analyze contrast-adjusted micrographs as described in Section 3.6.3. As shown in Figures 4.7 through 4.9, the area percent of voids in the microstructure increased with the amount of strain applied. The trend was approximately linear for the EHFF and EHDF samples at effective strains prior to necking and fracture

as evidenced by R^2 values of 0.9592 and 0.9927, respectively. The Nakazima samples did not trend in a very linear manner prior to fracture (R^2= 0.7576), but the void volume fraction increased with increasing strain, as was expected.

The steel used in this study showed visual evidence of banding, shown in Figure 5.1. As such, the DP600 steel supplied could be compared to banded DP600 steel in other work, shown in Figure 5.2. The trends of the void volume fraction data in Figures 4.7-10 were compared to data in literature [63], Figure 5.3. The data in the 0.0 to 0.7 range of effective strain in Figure 2.13 for DP600A showed a large amount of scatter with an increasing trend, which matches the increasing trend of the data in Figure 4.10. The strain data and void volume fraction were measured after failure.

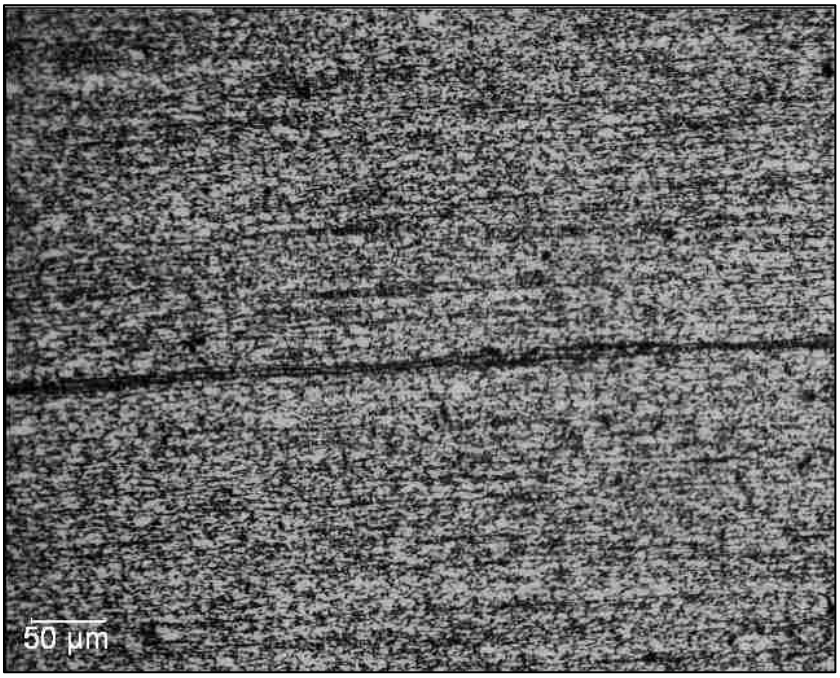

Figure 5.1: Martensite banding in DP600

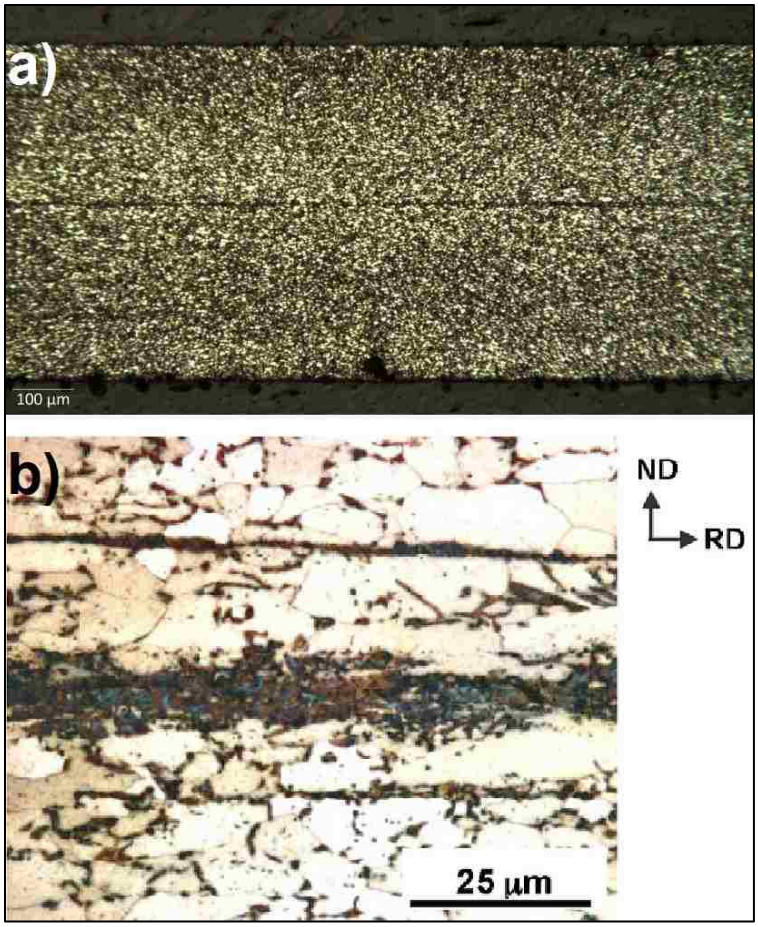

Figure 5.2: Banding in DP600 steel from a) DP600 steel 2 from Oliver (2010) [6]; b) DP600A from Avramovic-Cingara (2009) [63].

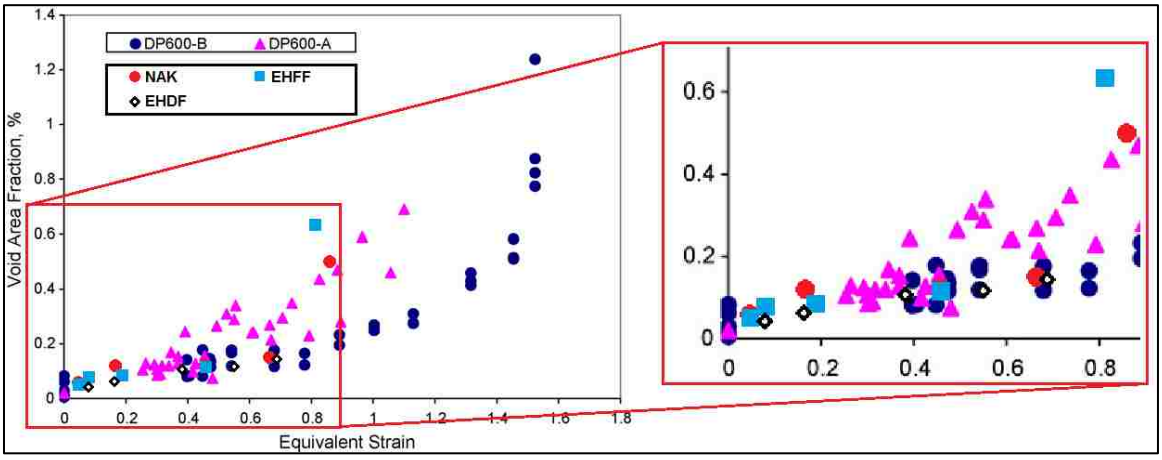

Figure 5.3: Current work compared to Avramovic-Cingara et al. [63]

Failure at the quasi-static rate of deformation followed the steps to failure outlined in Section 2.1.6. As the strain in the microstructure was increased, decohesion occurred between the ferrite and martensite grains. This effect is typically fully active at about 0.5% strain, which explains the onset of a rapid increase in void volume fraction evidenced by the change from an approximately linear trend to an exponential trend in Figure 4.7.

Figure 5.4a shows a sectioned view of the fracture of the Nakazima specimen. The expected v-shaped fracture is indicative of the 45 degree shear strain. The fracture appeared to initiate in the centre of the specimen where a linear pattern of voids is seen in the figure. The fracture profile exhibits multiple locations of similar cracking behaviour, because voids tend to coalesce and grow parallel to the applied load [30]. The fracture appeared to propagate through the thickness of the specimen at approximately 45° to the centre, which can be explained by the behaviour of slip lines in ferrite [25].

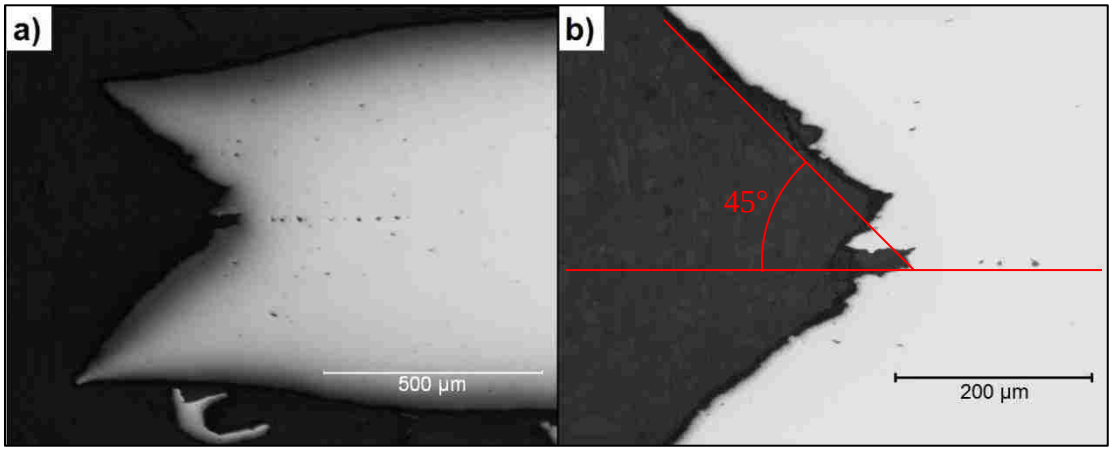

Figure 5.4: Fracture point of Nakazima specimen, a) 100x and b) 200x

A similar void accumulation pattern is seen in the literature, Figure 5.5 [63]. The reason for the greater void concentration at the centre of the specimen was related to the banded

martensite structure in the steel. The brittle martensite resisted the deformation to a greater extent than the ferrite, which caused decohesion at the ferrite/martensite interface.

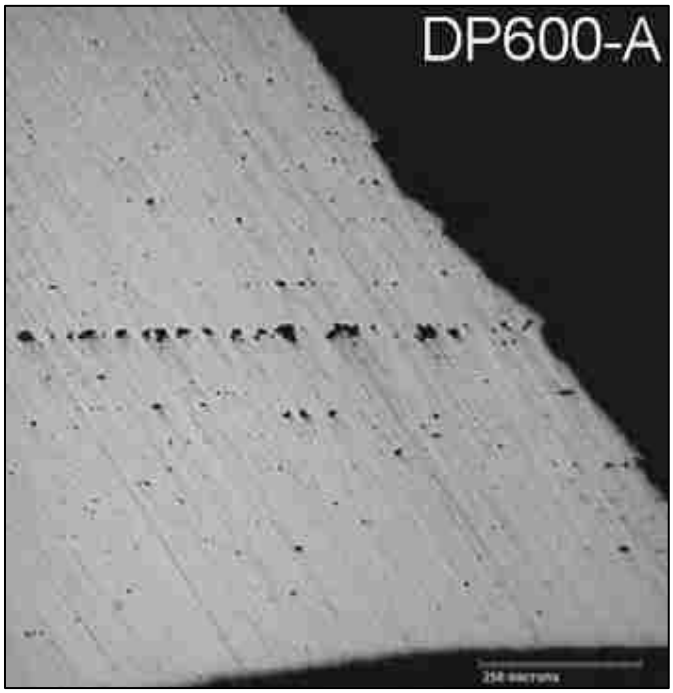

Figure 5.5: DP600 void accumulation [63]

In Figure 5.6, the voids near martensite particles are seen to have occurred predominantly at the grain interfaces between martensite and ferrite. Figure 5.7 shows, at a lower magnification, the distribution of voids along bands of martensite in the Nakazima specimen. It is clear in both of these micrographs that the dominant mechanism of failure in the DP600 during Nakazima testing was void nucleation and growth due to decohesion at martensite bands.

Some voids in Figure 5.6 occurred inside ferrite grains, particularly in the bottom third of the image, as opposed to directly adjacent to martensite at the interface. The strain gradient that exists from the centre of the ferrite grain to the boundary next to martensite

explains the presence of these voids. As stated in Section 2.1.6, undeformed ferrite exhibits a lower dislocation density than the ferrite surrounding martensite islands. This undeformed ferrite is harder than the ferrite containing initial dislocations, which creates a local stress concentration within the ferrite grain. This phenomenon was understood to be the cause of void nucleation and growth within the ferrite grains shown in Figure 5.6. These voids in the ferrite grains were quite small relative to those created due to decohesion at the ferrite/martensite interfaces. Their lesser size and frequency supports the theory that decohesion of the ferrite/martensite interfaces is the dominant fracture mechanism.

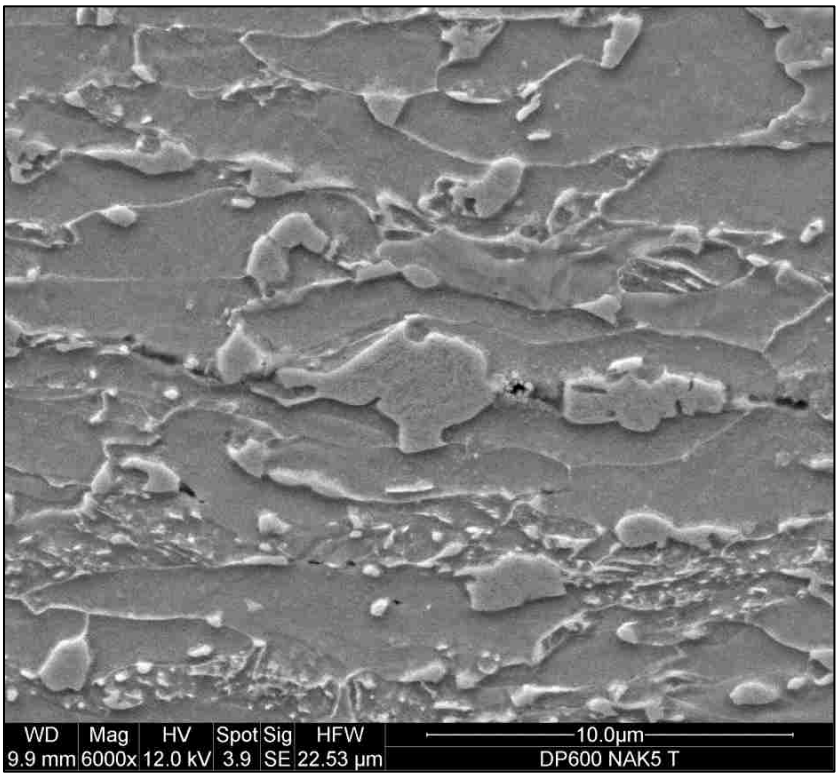

Figure 5.6: Voids concentrated at martensite particles

As mentioned above, decohesion at the ferrite/martensite interfaces was the dominant mechanism of failure in the Nakazima tests. The most popular sites for this to occur were

bands of martensite in the microstructure, as shown in Figure 5.7. The role of banding in fracture will be discussed later.

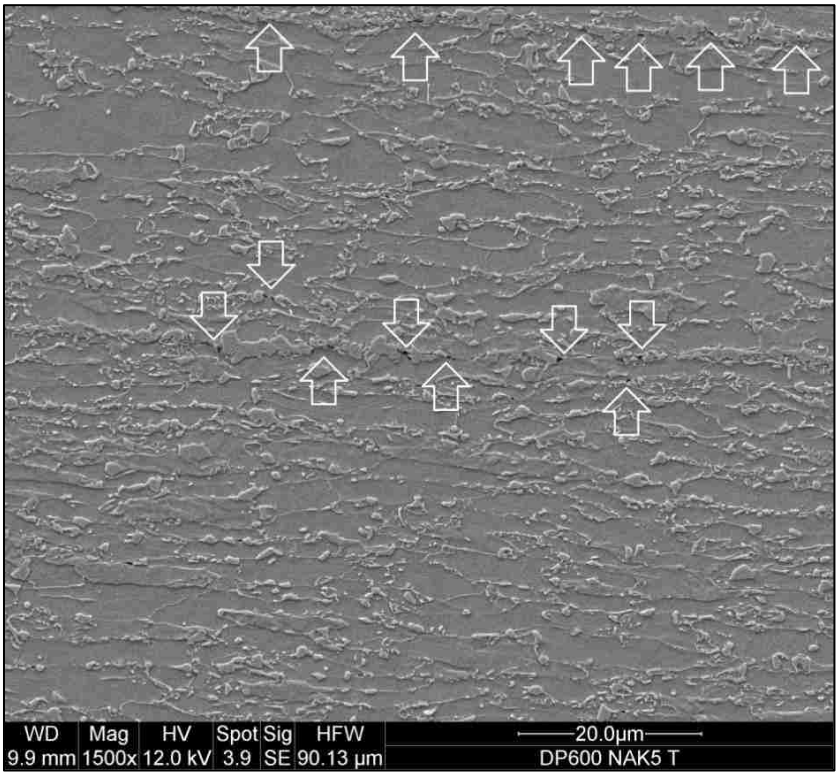

Figure 5.7: Arrows showing voids in martensite bands

Figure 4.8 illustrated the trend of void volume increase with increasing effective strain in the microstructure for the EHFF process. The safe strains were observed on a specimen formed at 14 kV and the specimen from which the fracture strain was measured was formed at 16 kV. As the trend line indicated, the void volume fraction increased exponentially and deviated from linear behaviour similar to the Nakazima specimen.

An increase in the number of voids in the area of fracture in the EHFF specimen is apparent in Figure 5.8. The voids increased in number and occurred closer together toward the area of fracture. Figure 5.8b shows the profile of the fracture, revealing the

evidence of void propagation at the fracture surface. It appeared as though the mechanism of fracture was similar to that in the Nakazima specimen, with deeper cracks towards the centre of the sheet. However, no large v-shaped fracture is noted macroscopically.

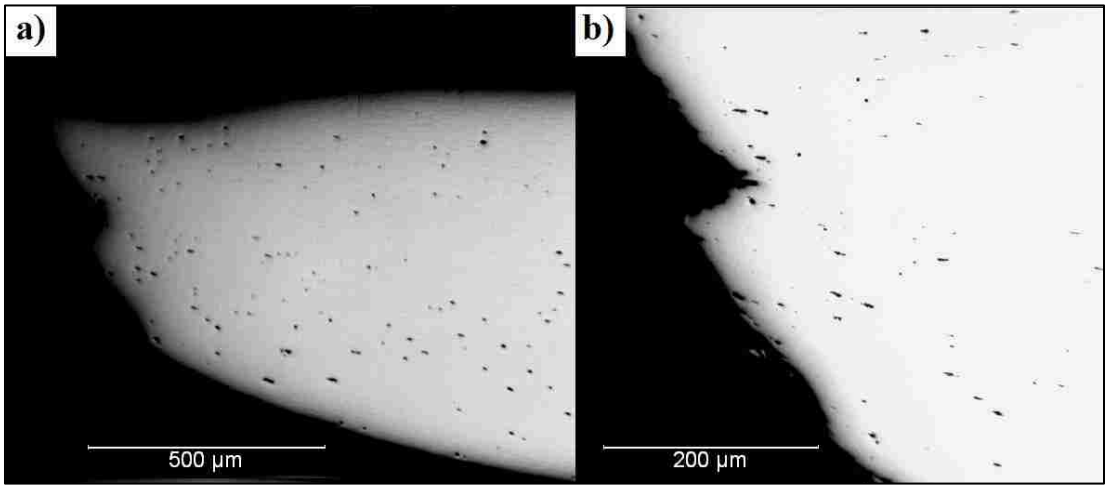

Figure 5.8: Fracture point of EHFF specimen, a) 100x and b) 200x

The void volume fraction increased approximately linearly with increasing strain in the EHDF specimen, as indicated in Figure 4.9. The safe strains shown were measured on a specimen formed at 12.2 kV using a ring that focused the shockwaves towards the centre of the sheet. Because no EHDF specimens failed in testing, the extreme case for EHDF was necking in the microstructure.

The neck in this case of EHDF was at lower strain than one would expect. It was not located at the apex of the specimen, but rather on the side of the formed cone. This specimen was formed at 15 kV without the aid of a ring. It was believed that the amount of energy used was not the sole cause of the neck, as the shape of the specimen was not the same as others that had enough energy to fill the die cavity. The non-focused

shockwave behaviour was believed to cause this premature localized neck in the specimen. Figure 5.9 shows the localized neck in the EHDF specimen.

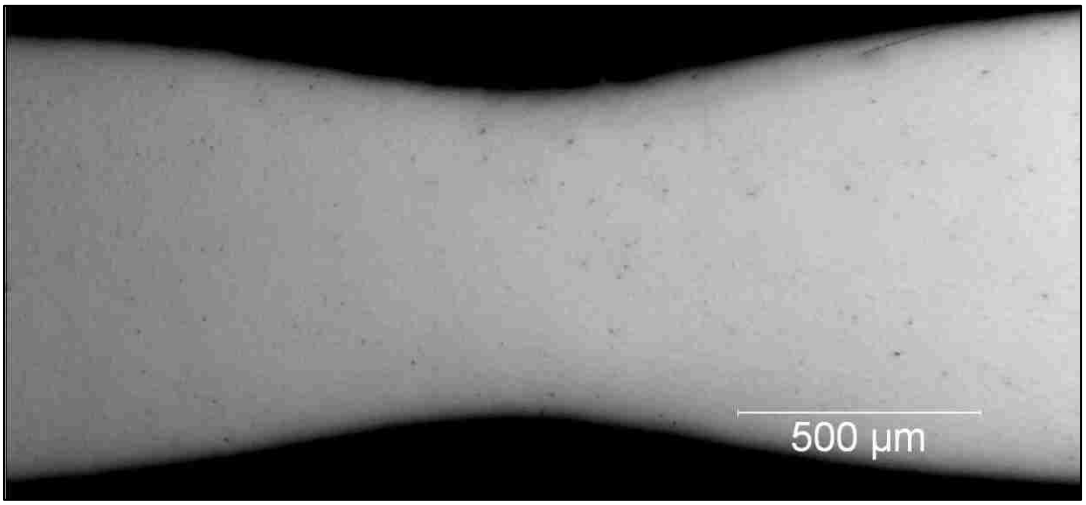

Figure 5.9: Necked area in EHDF specimen

The number of voids in the necked area was lower than in the Nakazima and EHFF cases due to the fact that the EHDF process experiences a different strain path that suppresses void growth. Section 2.2.4 described the deformation process of EHDF as including a stage of inertial effects as well as large compressive and shear forces upon die impact. As shown in Figure 2.12, the high velocity die impact creates large compressive forces, which interrupt the process of void growth through the thickness of the specimen. The effect of compressive stresses on the stress state was the cause of delayed damage in the microstructure; therefore the die impact in EHDF is the mechanism most responsible for void suppression compared to EHFF.

The increase in void volume fraction with increasing strain rate was shown in Figure 4.11. From this plot, it was clear that the EHDF process saw much higher peak strain rates across the entire sheet compared to those in EHFF. It should be noted that the four

peak strain rate values for each process were estimates for the midpoints of the metallographic samples numbered 2, 5, 8, and 11 for each specimen. Figure 4.11 showed the result of the die effect described above: the impact of the sheet with the die allows the DP600 steel to be formed at higher strain rates than in the EHFF process while suppressing failure throughout.

Figure 2.13 was modified with the data from Figure 4.10 and the result is shown in Figure 5.3. This shows that the data from Avramovic-Cingara et al. [63] for DP600-A and the data in this study fit relatively well.

The Nakazima specimen began forming voids at a higher rate initially, compared to the other two forming methods. The EHDF specimen showed more resistance to failure with increased strain, as the void volume fraction showed no sign of entering an exponential increase in fraction in the data collected. In Nakazima forming, there was constant contact between the punch and sheet and the process was monitored; upon fracture, the process was stopped as soon as possible. The final strains were limited by the process in the Nakazima forming operation, whereas the EHFF process stopped when the energy of the pulse was expended, as mentioned above.

5.3 Grain Size

In Figure 4.12 and Figure 4.13, the grain sizes of the Nakazima, EHFF, and EHDF specimens were plotted as a function of their section numbers; these corresponded to increasing deformation with increasing section number, and therefore increasing strain.

Two methods were used according to ASTM E112-13, as described in the experimental procedures in Section 3.6.4. The results from the Clemex and planimetric methods were shown in Figure 4.12 and Figure 4.13, respectively; they showed a similar trend of decreasing grain size with increasing deformation. In Figure 4.14, the two grain size measurement methods were compared using the EHDF case. It was observed that the two methods yielded comparable results; therefore the results were deemed to be validated by one another. Additionally, the relative accuracy (%RA) for the Clemex measurements ranged between a minimum of 1.294% and a maximum of 6.213%; all of the values between were considered acceptable by ASTM standards because they were less than 10%.

In the current work, grain size was measured across the longitudinal face, perpendicular to the rolling direction of each mounted sample. The grain size decreased with increasing strain, Figure 4.15, primarily because of the aspect ratio of the grains in the longitudinal orientation. As deformation progressed, the material thinned through its thickness, causing a reduction in the normal direction by a greater amount than in the longitudinal direction. This correlation of grain size and strain level was interpreted as another metric by which deformation could be qualitatively observed in the microstructure. Figure 4.15 shows that the decrease in grain size follows an approximately linear trend in areas of safe strains where these measurements were taken.

5.4 Martensite Volume Fraction

Martensite volume fraction was quantified in the as-received DP600 sheet material according to ASTM E1245-03 (2008) as described in Section 3.6.5. Using Clemex Vision Pro, the martensite volume fraction was found to be 14.34%, shown in Table 4.2. This value was deemed acceptable on the basis of the validity of the method according to ASTM E1245 and %RA of 0.1970%, far below the maximum 10% for acceptable results.

DP steels with greater than 50% martensite are especially brittle, while steels with martensite volume fraction below 10% do not benefit from the DP strengthening mechanisms described in Chapter 2. The martensite volume fraction quantification of 14.34% indicates two things: First, the steel was sufficiently ductile for the forming processes to which it was subjected. Second, it had sufficient martensite to create a significant dislocation density in the ferrite matrix to take advantage of the dislocation pinning mechanism to promote continuous yielding behaviour and increased strength.

Further investigation was conducted at ArcelorMittal into the volume fractions of the phases present in the microstructure of the current alloy using different etching techniques than the one described in Section 3.6.5. Three etchants were used, each for the purpose of revealing a different phase in different trials: 2% Nital etchant was made from nitric acid and ethanol to reveal ferrite as light gray, as shown in Figure 5.10a; 4% Picral etchant was made from picric acid and ethanol, and was used to reveal bainite as black features in the microstructure in Figure 5.10b; and LePera etchant, made from sodium metabisulfite and picric acid in ethanol, was used to reveal martensite as white islands,

visible in Figure 5.10c. The benefit of these etchants was their ability to differentiate the second phases in ferrite; it was clear which phase was bainite and which phase was martensite in Figure 5.10b and c.

Using this method of etching, the phases were quantified as shown in Table 5.1 below. If these values are correct, the lack of 10% of a strengthening phase should have a noticeable effect on the physical properties of DP steel, particularly the work hardening behaviour, which it did not. While interesting to consider, the method of determining these values was not well documented. As such, the values obtained using standard ASTM methodologies are considered in this work. Documentation and examination of the results of alternate etchants are left to future work.

Phase	Ferrite	Martensite	Bainite
Volume Fraction (%)	92.0	4.7	3.3

Table 5.1: Volume fraction of phases in DP600 using various etchants [70]

The martensite volume fraction of 14.34% found in Section 4.4 was deemed acceptable according to ASTM E1245, as it satisfied the requirements for accuracy. This method has been accepted in the literature, and yielded comparable results to other DP600 sheets. The reported values of martensite volume fraction in those sheets were 14.1%, 16.2%, and 18.5% [6]. The second phase in DP steel is considered to be the harder phase. It is generally considered to be martensite, with small amounts of bainite and/or retained austenite within the martensite grains. Carbon has diffused out of ferrite during the intercritical annealing stage, and so the structure of martensite, and possibly bainite or

retained austenite, will be the location of the majority of the carbon in the microstructure [71]. Since the steel in this study is a dual phase steel and, as stated, the second phase will be considered to contain martensite with bainite and/or retained austenite, there is no need to disambiguate the phases for the purpose of this work; however, the quantification of these phases could be useful in modelling applications in future work.

Anecdotally, the forming behaviour of this coil of steel has been considered problematic. Indeed, the presence of any significant amount of bainite may indicate a slower than expected cooling rate. While the steel meets the specification for DP590 as per ASTM A1088 in terms of composition and mechanical properties, its forming behaviour speaks to the proprietary nature of each producer's heat treatment process. Process variability can be considerable in terms of peak temperatures and time, which can affect austenite fraction and homogeneity. As noted [6], the martensite volume fraction can vary, 14.1-18.5%, across different manufacturers of DP600 steel.

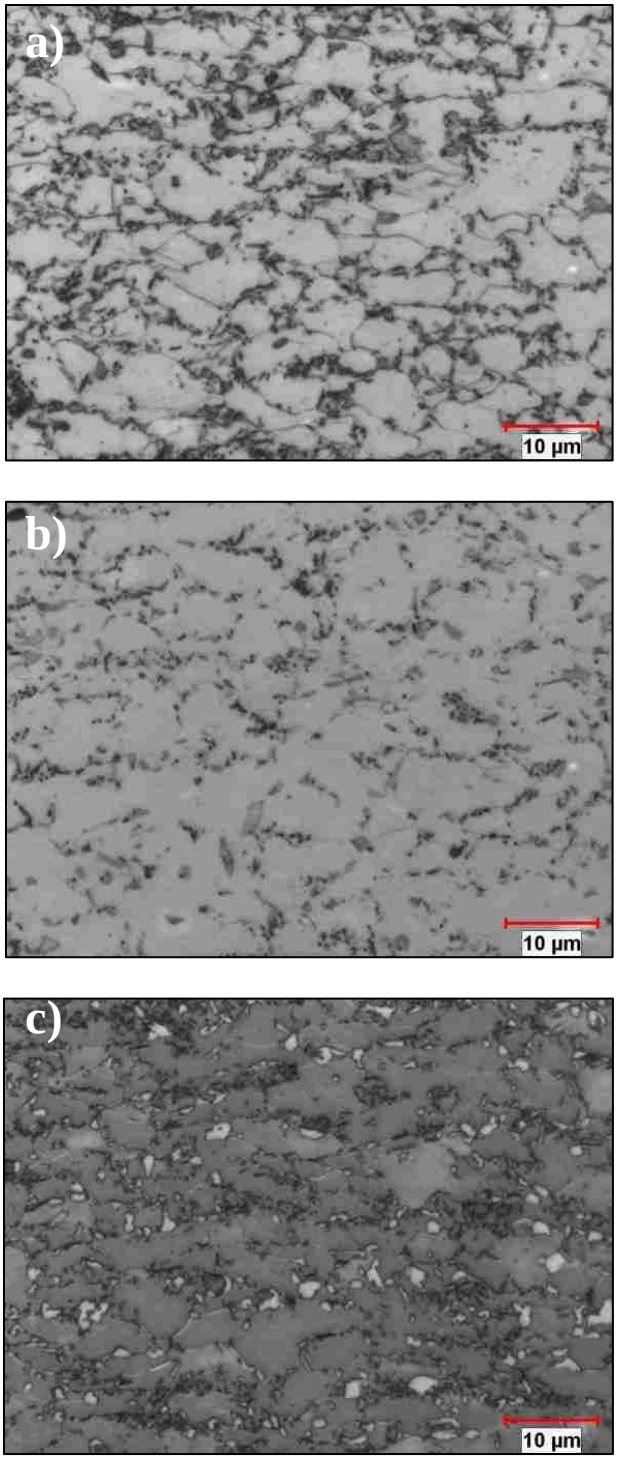

Figure 5.10: a) 2% Nital revealing gray ferrite; b) 4% Picral revealing black bainite; c) LePera revealing white martensite [70]

5.5 Fractography

SEM photos were taken of the fracture surfaces of the Nakazima and EHFF specimens to qualitatively observe the nature of fracture in the two different forming processes. The Nakazima specimen fracture was assumed to begin at the centre of the sheet thickness, as discussed in Section 5.2. The deepest part of the crack, Figure 5.4, was at the centre of the sheet and was understood to be due to the banding of martensite in the microstructure. Figure 5.11 shows the crack viewed using the SEM: the dotted lines outline the face of the crack, where the area above the top dotted line is the outer surface of the sample. Visible in the centre of the fracture face was a peak that ran the length of the crack that corresponded to the profile shown in Figure 5.4. Also visible in Figure 5.11 were a few surface features that appeared to be inclusions that could have accelerated the failure process.

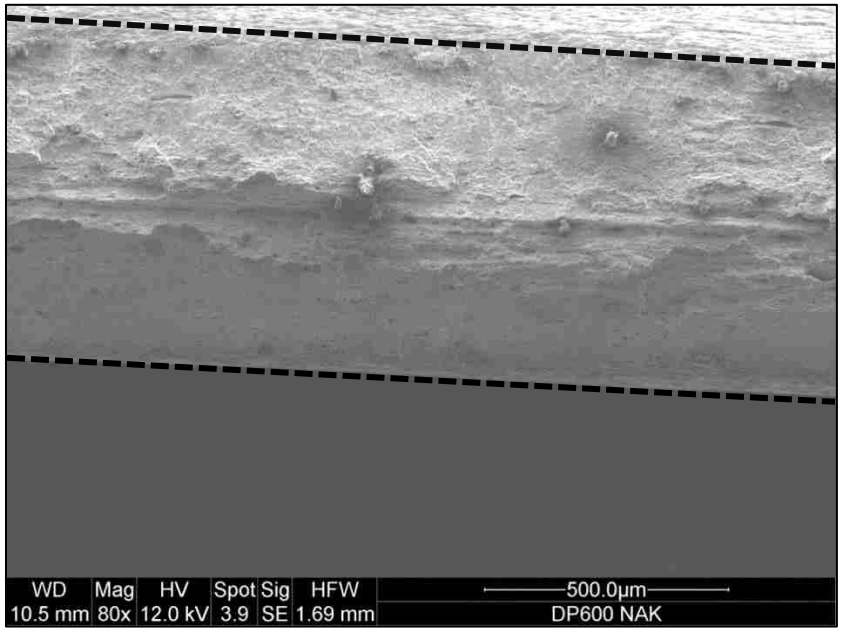

Figure 5.11: View of Nakazima fracture surface

It has been reported in literature that the surface features indicated in Figure 5.4 and Figure 5.11 are typical in cases of fracture in DP600 steel with banding under lower strain rate deformation. An example is shown in Figure 5.12, where the SEM micrograph showed evidence of a martensite band through the centre of the DP600 sheet causing damage similar to Figure 5.11 [6]. Also notable in the case of this figure was the martensite volume fraction of the steel, which was 16.2%; reasonably comparable to the 14.34% measured in the current work.

Figure 5.12: Fracture surface of banded DP600 steel 2 [6]

The roughness of the fracture surface is shown in Figure 5.13. The specimen failed in such a way that the centre of the fracture face exhibited peaks and valleys along its length. At the deepest areas of the fracture in Figure 5.13, it was observed that the main mechanism of failure resulted in deep cusps indicating ductile fracture.

Figure 5.14 is a higher magnification micrograph of the deep cusps of the fracture surface and the shape of the voids that led to fracture. It was observed that the majority of the voids appeared to be roughly spherical in shape across the fracture surface.

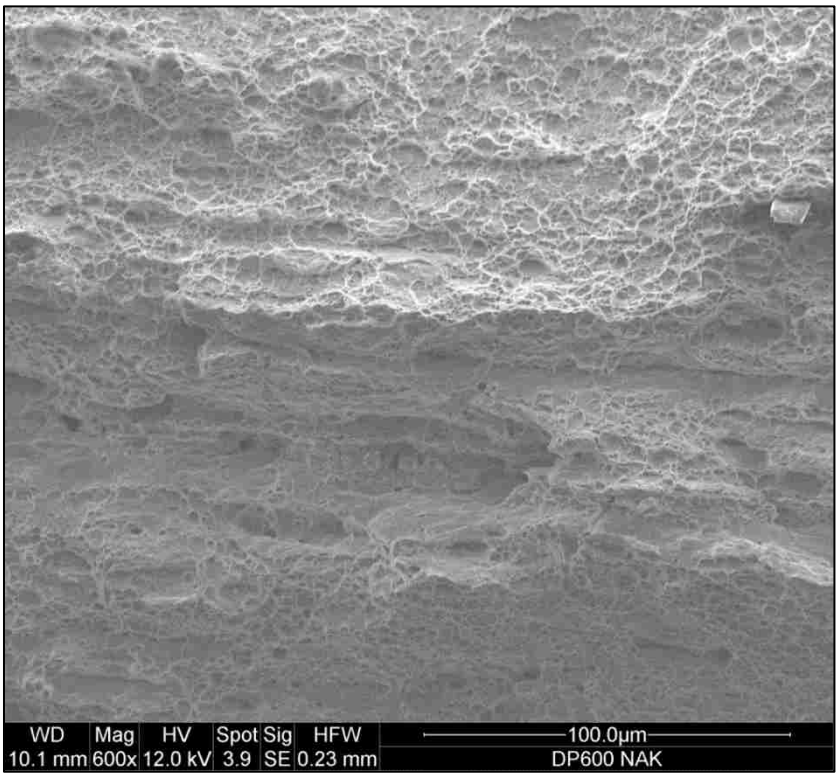

Figure 5.13: Nakazima fracture surface

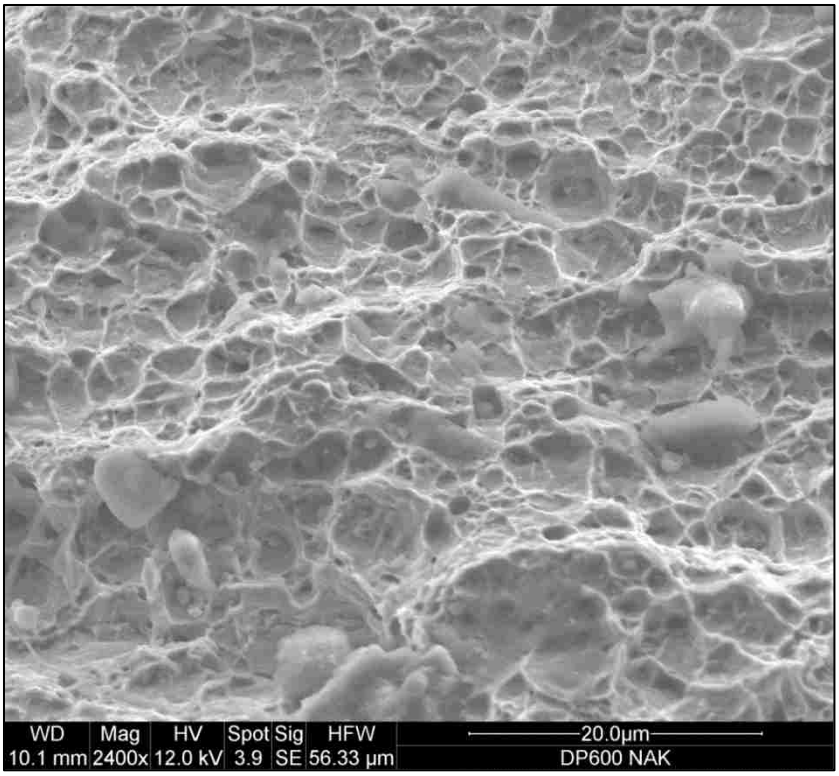

Figure 5.14: Nakazima fracture surface at higher magnification

Although the majority of the surface of the fracture face displayed deep cusps due to decohesion at the ferrite/martensite interface, there is also evidence of a smooth surface created by shearing during crack opening and propagation, Figure 5.15. The two mechanisms of decohesion and shear work in conjunction during the opening of a crack. This figure also displays the depth of the crack, more separation occurring above, and evidence of both elongated and spherical voids.

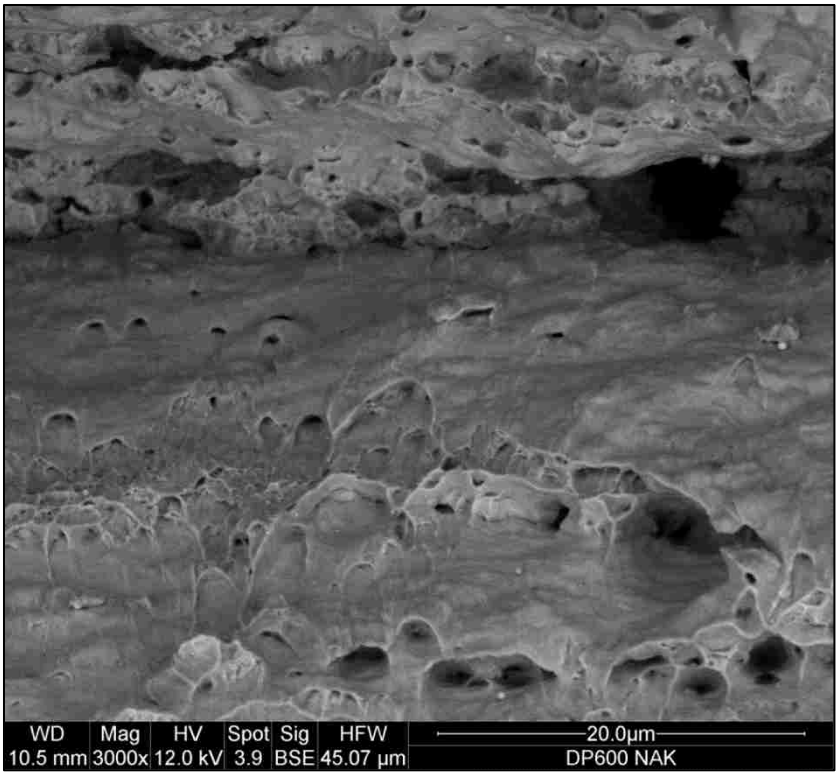

Figure 5.15: Inside of v-shaped fracture at centre of Nakazima specimen

In the EHFF specimen, the fracture surface did not display a central crack like in the Nakazima test. Figure 5.16 shows the EHFF fracture surface, revealing a number of deeper areas of damage as well as many visible voids. Although there was no central crack in the EHFF specimen, there was a region of deeper damage that appeared to occur on a plane through the fracture surface slightly above centre. Unlike the fracture of the Nakazima specimen, the EHFF specimen did not show the same amount of void accumulation at the martensite bands.

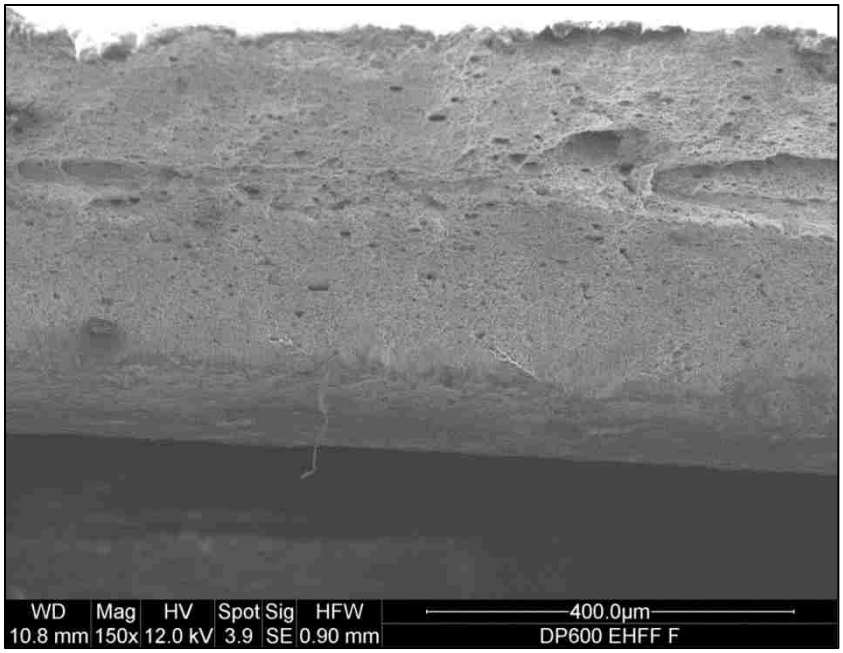

Figure 5.16: EHFF fracture surface

The deep crack in Figure 5.17 is shown using the backscatter electron image from the SEM to emphasize the volume of voids in the vicinity of fracture. It is evident in the figure that the majority of voids are smaller; there was also a mix of round and elongated ovular voids visible in the damaged area. Void coalescence was believed to have led to the elongated shape of the deep split that led to damage in this area; it appeared to be two large voids side by side that comprised the crack. In addition to the void formation and coalescence, the smooth surface of the crack where the split occurred was visible. This shear split was similar to that observed in Figure 5.15 for the Nakazima specimen.

Figure 5.17: Backscatter image of a crack in EHFF specimen

The EHFF specimen primarily failed in a ductile manner, evidenced in Figure 5.18 by deep cusps formed during grain boundary decohesion at the ferrite/martensite interface. The shallow, smooth areas are martensite grains that were cracked or caused ferrite to pull away. The shape of voids was observed to be both spherical and elongated in areas of fracture, with the majority being more equiaxed or spherical.

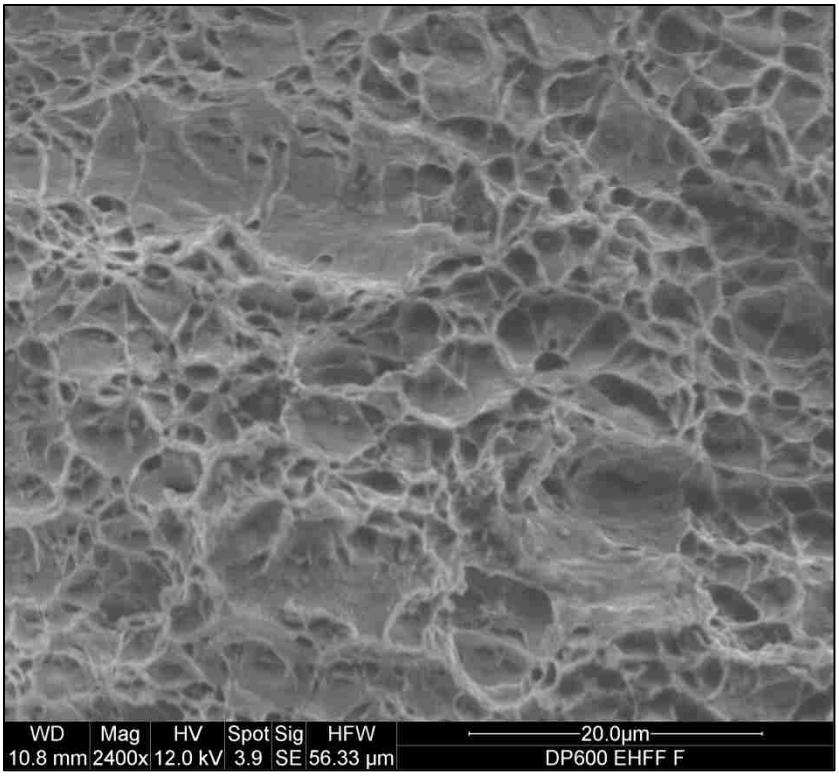

Figure 5.18: EHFF fracture surface

Chapter 6 :

Conclusions, Recommendations, and Contributions to the Field

6.1 Conclusions

1. The validation of the FMTI strain grid measurements with DIC data comparisons using Nakazima specimens allowed the FMTI system to be used with EHFF and EHDF specimens. Nakazima, EHFF, and EHDF strain values were consistently in the biaxial range, which allowed for valid comparison of the results for all three process variants throughout the study.

2. Void evolution in DP600 sheet steel follows a linear trend up to necking, at which point exponential void evolution behaviour is evident. This trend was confirmed by comparison to data in literature. The exponential trend was evident in the Nakazima and EHFF specimens and was more exaggerated in the latter. EHDF did not fracture, but showed a linear trend of void evolution.

3. Failure in Nakazima specimens was due to void nucleation and growth, which was focused at the centre of the sheet where a band of martensite was observed. The martensite did not deform at the same rate as the surrounding ferrite matrix, creating a strain gradient between the phases. The strain gradient eventually resulted in decohesion of the two phases, which nucleated voids around the martensite particles which grew, coalesced, and led to microcracks and failure. The failure at the

martensite band was compared to low strain rate testing in literature and matched those findings.

4. Grain size measurements according to ASTM E112 using both the planimetric method and manually using Clemex Vision Pro software were validated; therefore, either method can be used with confidence. These measurements were used to plot the change in the ferrite grain size with increasing strain in the microstructure. It was found that the ferrite grain size decreased in the longitudinal direction with increasing strain.

5. EHFF specimens failed in a ductile mode. However, comparison to void evolution in the Nakazima specimens demonstrated that high strain rate alone was clearly not enough to improve the resistance to void evolution. The greatest peak strain rate in EHFF was estimated to be 3820 s^{-1}, which was much lower than the greatest peak in EHDF.

6. The highest peak strain rate estimate in EHDF was 15340 s^{-1}, which was much greater than that estimated in EHFF. As expected, this high strain rate was accompanied by large compressive stresses upon impact with the die, which was the main cause for the suppressed void volume fraction evolution with increasing strain in the specimens in this study. It was determined that the EHDF process was able to successfully improve the formability of DP600 steel sheet according to the forming limit diagram in Figure 4.6.

7. Overall, three processes were used in the current work: Nakazima test, EHFF, and EHDF. The same material, DP600, was used in all three tests and yielded three different sets of results. The strain rate was lowest in the Nakazima test, in the range of 10^{-1} s^{-1}, and highest in the EHDF test, peaking at 15340 s^{-1}. The process used was determined to have the most significant effect on the formability improvement of the material, and the best formability was achieved using the EHDF process.

6.2 Recommendations for Future Work

1. Nakazima specimen strain data could be more consistent if tests were carried out to a specified punch displacement as opposed to relying on human operation based on video or data acquisition. An initial set of tests could be performed the same way as in this work to determine an approximate punch displacement at failure, and then the remaining tests could be performed to this punch displacement for consistency.

2. Grain size measurements could be segregated by orientation and used to calculate micro strains in separate phases to track microstructural deformation more closely. Micro strains in the phases can be measured at various locations in the microstructure and plotted to show which phase is most affected by strain. By measuring strain in the major and minor directions, the strain state of the material becomes clear. The practice of measuring the strains in this way has been used in literature [69].

3. Microhardness testing could be performed to determine the work hardening effect the EHDF process imparted on the steel during forming. Microhardness testing could be

performed on materials subject to all three forming processes. The results may show how much of an effect the conical die has on the hardness of each phase in the microstructure compared to the EHFF and Nakazima processes.

4. EHDF specimens should be tested to fracture to observe void volume fraction, fracture type, and effective strain at failure to compare to Nakazima and EHFF tests. By obtaining fracture data in the EHDF specimens, the strain at fracture could be compared to the void accumulation at the fracture point. This data could be plotted and compared to the other two processes for a complete summary of the fracture conditions.

5. The types and percentages of second phases in DP600 across several steel producers should be evaluated and related to the results to the formability of the steel. By comparing different DP600 steels, the effect of the varying martensite content and presence of bainite could be related to the mechanical properties and forming results.

6. The mean void size should be measured on specimens formed using all three processes to determine whether there is an effect of strain rate and/or die effect on the morphology of voids.

6.3 Unique Contributions to the Field

Dual phase steels are not a new alloy, nor is electrohydraulic die forming a new process; however, the current work contributes an understanding of a direct comparison of the biaxial deformation and fracture mechanisms of DP600 steel subject to quasi-static and

high strain rate forming processes. It indicates that the EHDF process allows increased formability due to void suppression. The data acquired in this work, particularly that obtained pertaining to voids in the microstructure, can be used in modelling applications to advance simulation and prediction of DP steel behaviour in the EHDF process. This will allow more accurate and successful part design for industry applications using EHDF.

A direct comparison of QS, EHFF, and EHDF test results provides a basis for quantifying the formability improvement associated with EHDF. This improvement is made clear when strain results are compared on an FLC for all processes. Using the data in this study, as well as that obtained from EHFF studies and QS testing, the formability improvement can be quantified in a definite way.

REFERENCES

1. Hulka K., "Modern Multi-Phase Steels for the Automotive Industry", Mater. Sci. Forum, 414-415, pp. 101-110, 2003.

2. Gilchrist I., Crossland B., "The Forming of Sheet Metal Using an Underwater Electrical Discharge", Proceedings of the Conference on Electrical Methods of Machining and Forming, 38, pp. 92-113, 1967.

3. Davies R. G., "Influence of Martensite Composition and Content on the Properties of Dual Phase Steels", Metallurgical Transactions A 9A, pp. 671-679, 1978.

4. Das D., Chattopadhyay P. P., "Influence of Martensite Morphology on the Work-Hardening Behaviour of High Strength Ferrite-Martensite Dual-Phase Steel", Journal of Materials Science, 44, pp. 2957-2965, 2009.

5. Smith W. F., Structure and Properties of Engineering Alloys, 2nd Edition, McGraw-Hill, 1993.

6. Oliver C., "Dual Phase Steel Characterization for Tube Bending and Hydroforming Applications", M.A.Sc Thesis, University of Windsor, Canada, 2010.

7. Speich G.R., Demarest V.A., and Miller R.L., "Formation of Austenite During Intercritical Annealing of Dual-Phase Steels", Metallurgical Transactions A, Physical Metallurgy and Materials Science, 12A(8), pp. 1419-1428, 1981.

8. Lanzillotto C.A.N. and Pickering F.B., "Structure-Property Relationships in Dual-Phase Steels", Metal Science, 16, pp. 371-382, 1982.

9. Balliger N.K. and Gladman T., "Work Hardening of Dual-Phase Steels", Metal Science, 15(3), pp. 95-108, 1981.

10. Westphal M., McDermid J.R., Boyd J.D., andEmbury J.D., "Novel Thermal Processing of Dual Phase Steels: I – Microstructural Design", Canadian Metallurgical Quarterly, 47, pp. 83-90, 2008.

11. Güral A., Bostan B., Özdemir A. T., "Heat Treatment in Two Phase Region and Its Effect on Microstructure and Mechanical Strength After Welding of a Low Carbon Steel", Materials and Design, 28, pp. 897-903, 2007.

12. He X.J., Terao N., and Berghezan A., "Influence of Martensite Morphology and

its Dispersion on Mechanical Properties and Fracture Mechanisms of Fe-Mn-C Dual Phase Steels", Metal Science, 18, pp. 367-373, 1984.

13. Wang Z., Zhao A., Zhao Z., Ye J., Tang D., and Zhu G., "Microstructures and Mechanical Properties of C-Mn-Cr-Nb and C-Mn-Si-Nb Ultra-High Strength Dual-Phase Steels", International Journal of Minerals, Metallurgy, and Materials, 19(10), pp. 915-922, 2012.

14. Davies R. G., "Influence of Silicon and Phosphorous on the Mechanical Properties of Both Ferrite and Dual-Phase Steels", Metallurgical Transactions A, 10A, pp. 113-118, 1979.

15. Smallman, R. E., and Bishop R. J., Modern Physical Metallurgy and Materials Engineering, 6th Edition. Woburn, MA: Butterworth-Heinemann, 1999.

16. Majka T. F., Matlock D. K., and Krauss G., "Development of Microstructural Banding in Low-Alloy Steel with Simulated Mn", Metallurgical and Materials Transactions A 33A, pp. 1627-1637, 2002.

17. Caballero F. G., García-Junceda A., Capdevila C., and García de Andrés C., "Evolution of Microstructural Banding During the Manufacturing Process of Dual Phase Steels", Materials Transactions 47(9), pp. 2269-2276, 2006.

18. McGarrity K. S., Sietsma J., and Jongbloed G., "Characterisation and Quantification of Microstructural Banding in Dual Phase Steels Part 1 – General 2D Study", Institute of Materials, Minerals and Mining 28(8), pp. 895-902, 2012.

19. Fischmeister H., Karlsson B., "Plastizitaetseigenschaften grob-zweiphasiger werkstoffe", Z. Metallkde, 68(5), pp. 311-327, 1977.

20. Nishiyama Z., Martensitic Transformation, Academic Press, New York, 1978.

21. Bergström Y., Granbom Y., and Sterkenburg D., "A Dislocation-Based Theory for the Deformation Hardening Behaviour of DP Steels: Impact of Martensite Content and Ferrite Grain Size", Journal of Metallurgy, 210, pp. 1-16, 2010.

22. Hull D. and Bacon D.J., Introduction to Dislocations, 3rd Edition. New York, NY: Pergamon Press, 1984.

23. Kumar A., Singh S.B., and Ray K.K., "Influence of Bainite/Martensite Content on the Tensile Properties of Low Carbon Dual-Phase Steels", Materials Science and Engineering A, 474, pp. 270-282, 2008.

24. Mazinani M. and Poole W.J., "Effect of Martensite Plasticity on the Deformation Behaviour of a Low-Carbon Dual-Phase Steel", Metallurgical and Materials

Transactions A, 38A, pp. 328-339, 2007.

25. Shen H.P., Lei T.C., and Liu J.Z., “Microscopic Deformation Behaviour of Martensitic-Ferritic Dual-Phase Steels”, Materials Science and Technology, 2, pp. 28-33, 1986.

26. Tsipouridis P., “Mechanical Properties of Dual-Phase Steels”, Thesis, 2006.

27. Callister D.W. Jr., Materials Science and Engineering An Introduction, 7th Edition. New York, NY: John Wiley & Sons, Inc., 2007.

28. Matlock D. K., and Speer J. G., “Processing Opportunities for New Advanced High-Strength Sheet Steels”, Materials and Manufacturing Processes, 25, pp. 7-13, 2010.

29. Cribb W.R., and Rigsbee J.M., “Work-Hardening Behaviour and its Relationship to the Microstructure and Mechanical Properties of Dual-Phase Steels”, IEEE Conference Record of Annual Pulp and Paper Industry Technical Conference, pp. 91-117, 1981.

30. Steinbrunner D. L., Matlock D. K., and Krauss G., "Void Formation During Tensile Testing of Dual Phase Steels", Metallurgical and Materials Transactions A 19(3), pp. 579-589, 1988.

31. Szewczyk A.F. and Gurland J., “A Study of the Deformation and Fracture of Dual-Phase Steel”, Metallurgical Transactions A, 13A, pp. 1821-1826, 1982.

32. Altan, T. (Ed.), Schuler: Metal Forming Handbook. Berlin, Germany: Springer-Verlag, 1998.

33. Torkar M., Tehovnik F., Podgornik B., “Failure Analysis at Deep Drawing of Low Carbon Steels”, Engineering Failure Analysis, 40, pp. 1-7, 2014.

34. Nakazima K., Kikuma T., and Hasuka K., "Study on the formability of steel sheets", Yawata Technical Report No. 284, pp. 140-141, 1968.

35. Fazli A. and Arezoo B., “An Analytical Method of Prediction of Limiting Draw Ratio for Redrawing Stages of Axisymmetric Deep Drawn Components”, Journal of Manufacturing Science and Engineering, 136, pp. 1-10, 2014.

36. Lang L.H., Wang Z.R., Kang D.C., Yuan S.J., Zhang S.H., Danckert J., and Nielsen K.B., “Hydroforming Highlights: Sheet Hydroforming and Tube Hydroforming”, Journal of Materials Processing Technology, 151, pp. 165-177, 2004.

37. Bagherzadeh S., Mollaei-Dariani B., and Malekzadeh K., "Theoretical Study on Hydro-Mechanical Deep Drawing Process of Bimetallic Sheets and Experimental Observations", Journal of Materials Processing Technology, 212(9), pp. 1840-1849, 2012.

38. Aust M., "Modified Hydromechanical Deep Drawing", Proceedings of the International Conference on Hydroforming, pp. 215-234, 2001.

39. Nakamura K. and Nakagawa T., "Radial Pressure Assisted Hydraulic Counter Pressure Deep Drawing, Journal of the Japan Society for Technology of Plasticity, 26(228), pp. 73-78, 1985.

40. Kolleck R. and Cherek H., "Active Hydromechanical Deep Drawing A New Process For Lightweight Design Manufacturing", Proceedings of the SheMet International Conference, pp. 177-182, 2001.

41. Seth M., Vohnout V.J., and Daehn G.S., "Formability of Steel Sheet in High Velocity Impact", Journal of Materials Processing Technology, 168, pp. 390-400, 2005.

42. Priem D., Marya S., and Racineux G., "On the Forming of Metallic Parts Through Electromagnetic and Electrohydraulic Processing", Advanced Materials Research, 15-17, pp. 655-660, 2007.

43. Hasebe T., Takenaga Y., Kakimoto H., and Imaida Y., "High Strain Rate Forming Using an Underwater Shock Wave Focusing Technique", Journal of Materials Processing Technology, 85, pp. 194-197, 1999.

44. Psyk V., Risch D., Kinsey B.L., Tekkaya A.E., and Kleiner M., "Electromagnetic Forming – A Review", Journal of Materials Processing Technology, 211(5), pp. 787-829, 2011.

45. Rohatgi A., Stephens E.V., Soulami A., Davies R.W., and Smith M.T., "Experimental Characterization of Sheet Metal Deformation During Electro-Hydraulic Forming", Journal of Material Processing Technology, 211(11), pp. 1824-1833, 2011.

46. Rohatgi A., Stephens E.V., Davies R.W., Smith M.T., Soulami A., and Ahzi S., "Electro-Hydraulic Forming of Sheet Metals: Free-Forming vs. Conical-Die Forming", Journal of Materials Processing Technology, 212(5), pp. 1070-1079, 2012.

47. Balanethiram V.S. and Daehn G.S., "Enhanced Formability of Interstitial Free Iron at High Strain Rates", Scripta Metallurgica et Materiala, 27(12), pp. 1783-1788, 1992.

48. Balanethiram V.S., Hu X., Altynova M., and Daehn G.S., “Hyperplasticity: Enhanced Formability at High Rates”, Journal of Materials Processing Technology, 45(1-4), pp. 595-600, 1994.

49. Daehn G.S., Altynova M., Balanethiram V.S., Fenton G., Padmanabhan M., Tamhane A., and Winnard E., “High-velocity Metal Forming – An Old Technology Addresses New Problems”, Journal of Materials, 47(7), pp. 42-45, 1995.

50. Golovashchenko S., Mamutov V., Dmitriev V., and Sherman A., “Formability of Sheet Metal With Pulsed Electromagnetic and Electrohydraulic Technologies”, Proceedings of TMS Symposium “Aluminum-2003”, pp. 99-110, 2003.

51. Golovashchenko S.F., Gillard A.J., and Mamutov A.V., “Formability of Dual-Phase Steels in Electrohydraulic Forming”, Journal of Materials Processing Technology, 213(7), pp. 1191-1212, 2013.

52. Mynors D.J. and Zhang B., “Applications and Capabilities of Explosive Forming”, Journal of Materials Processing Technology, 125-126, pp.1-25, 2002.

53. Imbert J., Winkler S.L., Worswick M.J., Olivera D.A., and Golovashchenko S., “The Effect of Tool-Sheet Interaction on Damage Evolution in Electromagnetic Forming of Aluminum Alloy Sheet”, Journal of Engineering Materials and Technology, 127, pp. 145-152, 2005.

54. Chu Y.Y., Lee R.S., Psyk V., and Tekkaya A.E., “Determination of Flow Curve at High Strain Rates Using Electromagnetic Punch Stretching”, Journal of Materials Processing Technology, 212(6), pp. 1314-1323, 2012.

55. Melander A., Delic A., Björkblad A., Juntunen P., Samek L., and Vadillo L., “Modelling of Electro Hydraulic Free and Die Forming of Sheet Steels”, International Journal of Material Forming, 6(2), pp. 223-231, 2013.

56. Tobe T., Kato M., and Obara H., “Metal Forming by Underwater Wire Explosions 2. Experiments on Bulging of Circular Aluminum Sheets by Copper Wire Explosions”, Bulletin of the JSME, 27(223), pp. 130-135, 1984.

57. Vivek A., Kim K.-H., and Daehn G.S., “Simulation and Instrumentation of Electromagnetic Compresion of Steel Tubes”, Journal of Materials Processing Technology, 211(5), pp. 840-850, 2011.

58. Kleiner M., Beerwald C., and Homberg W., “Analysis of Process Parameters and Forming Mechanisms With the Electromagnetic Forming Process”, CIRP Annals of Manufacturing Technology, 54(1), pp. 225-228, 2005.

59. Cui X.-H, Mo J.-H, and Zhu Y., "3D Modeling and Deformation Analysis for Electromagnetic Sheet Forming Process", Transactions of Nonferrous Metals Society of China, 22(1), pp. 164-169, 2012.

60. Hassannejadasl A., Green D.E., Golovashchenko S.F., Samei J., and Maris C., "Numerical Modelling of Electrohydraulic Free-Forming and Die-Forming of DP590 Steel", Journal of Manufacturing Processes, 16(3), pp. 391-404, 2014.

61. Golovashchenko S.F., and Mamutov V.S., "Electrohydraulic Forming of Automotive Panels", Proceedings of 6th Global Innovations Symposium: Trends in Materials and Manufacturing Technologies for Transportation Industries, pp. 65-70, 2005.

62. Golovashchenko S.F., "Material Formability and Coil Design in Electromagnetic Forming", Journal of Materials Engineering and Performance, 16(3), pp. 314-320, 2007.

63. Avramovic-Cingara G., Ososkov Y., Jain M.K., and Wilkinson D.S., "Effect of Martensite Distribution on Damage Behaviour in DP600 Dual Phase Steels", Materials Science and Engineering A, 516(1-2), pp. 7-16, 2009.

64. ASTM Standard A1088, 2013, "Standard Specification for Steel, Sheet, Cold-Rolled, Complex Phase (CP), Dual Phase (DP) and Transformation Induced Plasticity (TRIP)," ASTM International, West Conshohocken, PA, 2013, DOI: 10.1520/A1088-13, www.astm.org.

65. Turkoz M., Osman Y., Dilmec M., and Halkaci H.S., "Construction of Forming Limit Diagrams for AA 5754 and AA 2024 Aluminum Alloys", Proceedings of the 12th International Conference on Aluminum Alloys, The Japan Institute of Light Metals, pp. 516-521, 2010.

66. ASTM Standard E1245, 2003, "Standard Practice for Determining the Inclusion or Second-Phase Constituent Content of Metals by Automatic Image Analysis," ASTM International, West Conshohocken, PA, 2008, DOI: 10.1520/E1245-03R08, www.astm.org.

67. ASTM Standard E112, 2013, "Standard Test Methods for Determining Average Grain Size," ASTM International, West Conshohocken, PA, 2013, DOI: 10.1520/E0112-13, www.astm.org.

68. Hassannejadasl A., Unpublished notes, University of Windsor, 2014.

69. Samei J., "Multi-scale Characterization of Hyperplasticity and Failure in Dual-Phase Steels Subject to Electrohydraulic Forming", PhD Dissertation, University

of Windsor, Canada, 2013.

70. Samei J., Unpublished notes, University of Windsor, 2013.

71. Leslie W.C., and Sober R.J., “The Strength of Ferrite and Martensite as Functions of Composition, Temperature, and Strain Rate”, Trans. ASM, 60, pp. 459-484, 1967.

VITA AUCTORIS

NAME:	Brent Richard Charles McCallum
PLACE OF BIRTH:	London, Ontario
YEAR OF BIRTH:	1989
EDUCATION:	Bachelor of Applied Science Honours Mechanical Engineering with Materials Option University of Windsor Windsor, Ontario 2011 Master of Applied Science Engineering Materials University of Windsor 2014